INVESTIGATION OF GAUSSIAN BEAM PROPAGATION METHODS AND ANALYSIS OF THE HSX TRANSMISSION LINE WITH SMOOTH-WALL AND PERTURBED-WALL LAUNCHERS

by

Eric Buscarino

A thesis submitted in partial fulfillment of

the requirements of the degree of

Master of Science

(Electrical and Computer Engineering)

at the

UNIVERSITY OF WISCONSIN – MADISON

2013

Abstract

Gaussian beams are electromagnetic waves with Gaussian distribution amplitudes in the transverse directions and are important for electron cyclotron heating (ECRH) in many plasma fusion experiments. Systems that have the ability to transform the non-Gaussian output of some gyrotrons are of particular interest and it is important to understand the limits of the methods used in designing and simulating these systems.

The computational propagation of Gaussian beams is important in the design and modeling of complex and high-power systems. Therefore it is important to understand the limits of where current approximate analytical solutions and computational methods differ. The first objective of this thesis is to analyze two computational methods of propagation, the Fourier Transform method and the Finite-Difference Time-Domain method, and compare the results to the paraxial approximation solution for Gaussian beams. Specifically, these methods are tested for initial beam waist radii in the region of a wavelength or less than a wavelength. It was found that there was good agreement between each method and that it would be advisable to use FFT for narrow beam free-space propagation and FDTD for domains consisting of scatterers.

A perturbed-wall launcher designed by Ungku Fazri Ungku Farid was implemented in the HSX microwave transmission system and simulated using Surf3d. The original smooth-wall Vlasov launcher HSX microwave transmission system was also simulated and found to have 63% of the input power propagated to the dual-mode waveguide, while the perturbed-wall launcher only propagated less than 10%. The original launcher also propagated a beam to the dual-mode waveguide containing

significantly more Gaussian content than the perturbed-wall launcher beam. This significant performance decrease is due to the HSX microwave transmission system being designed using geometrical optics for shaping the output beam of the smooth-wall Vlasov launcher and, if redesigned for the perturbed-wall launcher, the system could realize increased propagated power. For the perturbed-wall system there should be less power loss and less spillover loss in the system due to a better output beam from the launcher.

Acknowledgements

I would like to thank the many people who have helped and supported me during my time at the University of Wisconsin-Madison.

First and foremost, I would like to express my deep appreciation and gratitude to my advisor Professor Ronald J. Vernon for his support, guidance, and patience. Prof. Vernon helped me develop the ability to ask the right questions when facing unexpected results and to develop a step-by-step thinking process with independent research attitude. I am particularly grateful for his patience and encouragement throughout my time in his group especially during the last few months of writing this thesis.

I would also like to thank Konstantin Liken and Ungku Fazri Ungku Farid for the guidance in my work on the HSX transmission system. Fazri's willingness to provide guidance and advice despite his own heavy workload on which a large portion of this thesis is based is deeply appreciated. The guidance that Ben Rock provided during my first few months in the group helped me get my work pointed in the right direction and I would like to thank Brian Fox for always being willing to help point me in the right direction when issues arose in my work.

Additionally, I would like to thank my mother Karen Donoughe, my father Michael Buscarino, my stepmother Jeanne Buscarino, and my stepfather Tom Donoughe for their constant support and encouragement.

Finally, I'd like to thank the Department of Energy for funding this research through contract DE-FG02-85ER52122.

Table of Contents

Chapter 1

Introduction

1.1 Introduction to Gaussian Beams

A Gaussian beam is an electromagnetic wave in which the transverse amplitude and phase are Gaussian distributions. A very important application of Gaussian beams is in electron cyclotron resonance heating (ECRH) used in many plasma fusion research projects such as the W7-X stellarator at IPP-Greifswald and the DIII-D tokamak at General Atomics [1-2]. The application of full beam analysis will be studied in this thesis through the application of beam propagation methods to the Helically Symmetric eXperiment (HSX), a quasihelically symmetric (QHS) stellarator at the University of Wisconsin-Madison [3].

Plane-wave spectrum analysis is a common method for treating Gaussian beam propagation. This method represents a Gaussian beam as an ensemble of plane waves given by the Gaussian spatial distribution function. The behavior of the Gaussian beam is treated as a linear superposition of the ensemble of plane waves. While each component of the ensemble satisfies the classical theory of reflection and transmission, the linear superposition of these components generally does not exactly follow the path given by geometric optics [4]. This behavior is the main focus of the material presented in this thesis.

Several key parameters describe the key properties of interest in a propagating Gaussian beam. Fig. 1.1.1 below shows a general propagating Gaussian beam in free space.

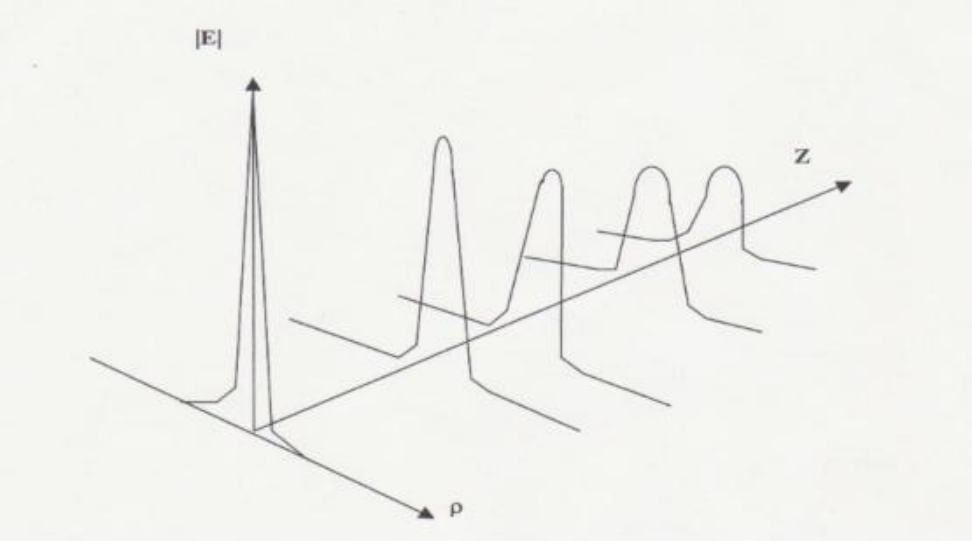

Figure 1.1.1: Amplitude of one-dimensional Gaussian beam propagating in the +z-direction.

A defining feature of a beam is the initial waist radius, w_0, and is defined as the radial distance to the point of -8.7 dB. As the beam propagates, the beam radius spreads in the plane perpendicular to the direction of propagation and is described as a function of propagation distance *w(z)* for propagation in the *+z* direction. The radius of curvature *R(z)* is a general characteristic of propagation and is the curvature of the constant phase surfaces of the beam. These properties can be expressed in analytical expressions in approximate solutions for a propagating Gaussian beam.

This thesis contains two separate investigations of Gaussian beam propagation. Chapter 2 investigates the accuracy of the Fast-Fourier Transform method and the Finite-Difference Time-Domain method in propagating Gaussian beams as well as a discussion of each method's inherent strengths and weaknesses. In Chapter 3 the HSX microwave transmission system is analyzed using the Surf3d computational software. The HSX transmission system using a smooth-wall Vlasov launcher is analyzed and compared to

experimental measurements. In addition to analyzing the HSX microwave transmission system as it is currently implemented, it is also simulated and analyzed with the smooth-wall Vlasov launcher replaced by the perturbed-wall launcher designed by U. F. Ungku Farid [5].

Chapter 2

Beam Propagation Method Analysis

In this chapter a comparison of the paraxial approximate solution of a propagating Gaussian beam is compared to the results of a Gaussian beam propagated using the Fourier Transform method and the Finite-Difference Time-Domain method. These comparisons focus on the case where the initial beam radius is one wavelength or less.

2.1 Paraxial Approximation Solution

A full-wave analytical solution to a propagating Gaussian beam has proven difficult to find [4]. One method of approximating the behavior of a propagating beam is to find the solution to the vector Helmholtz equation under paraxial conditions. Another method of analysis is the plane-wave spectrum analysis. Plane-wave spectrum analysis uses linear-superposition of an ensemble of plane waves to represent a beam. Applying the Fourier transform to this ensemble provides analytical solutions to beam propagation under certain conditions. This section presents the paraxial solution and the following section presents the Fourier transform method

The propagation of a Gaussian beam in free space is governed by the Helmholtz wave-equation

$$\nabla^2\mathbf{E} + \boldsymbol{k}^2\mathbf{E} = \mathbf{0} \qquad (2.1.1)$$

where **E** is the electric field, but could be any of the electromagnetic fields *E*, *H*, or *A* and the wave number $k = \omega\sqrt{\mu\varepsilon}$. For a beam propagating in the +z direction Eq. 2.1.1 may be rewritten as

$$\nabla_t^2 E + \frac{\partial^2 E}{\partial z^2} + k^2 E = 0 \tag{2.1.2}$$

where the transverse scalar Laplacian operator in cylindrical coordinates is given by

$$\nabla_t^2 E = \frac{1}{\rho}\frac{\partial}{\partial \rho}\left(\rho \frac{\partial E}{\partial \rho}\right) + \frac{1}{\rho^2}\frac{\partial^2 E}{\partial \phi^2}. \tag{2.1.3}$$

Solutions of Eq. 2.1.2 will be of the form

$$E(\rho, \phi, z) = \psi(\rho, \phi, z) e^{-jkz}, \tag{2.1.4}$$

where ψ is a slowly varying function of z and rapid variation of *E* is assumed to only be due to the exponential term. Substituting Eq. 2.1.4 into Eq. 2.1.2 and using the paraxial approximation that ψ is a slowly varying function of z compared to e^{-jkz}, then Eq. 2.1.2 becomes

$$\nabla_t^2 \psi - j2k\frac{\partial \psi}{\partial z} \approx 0. \tag{2.1.5}$$

The approximate equation given in Eq. 2.1.5 is called the paraxial equation.

From this approximation of the vector Helmholtz equation the modal paraxial solution for Gaussian beams is found. Possible solutions to Eq. 2.1.5 of the form,

$$\psi = exp\left[-j\left(p + \frac{k}{2q}\rho^2\right)\right], \tag{2.1.6}$$

can be found where $p(z)$ is a complex phase shift associated with the propagating wave and $q(z)$ is a complex beam parameter describing the variation in the amplitude of the beam a distance ρ from the z-axis. In the following the method for deriving the TEM_{00} mode will be demonstrated but other higher order modes can also be found.

For the TEM_{00} mode propagating in the +z-direction the transverse electric field takes the form of,

$$E(\rho, z) = E_0 \frac{w_0}{w(z)} e^{-\rho^2/w^2(z)} \Phi(\rho, z), \tag{2.1.7}$$

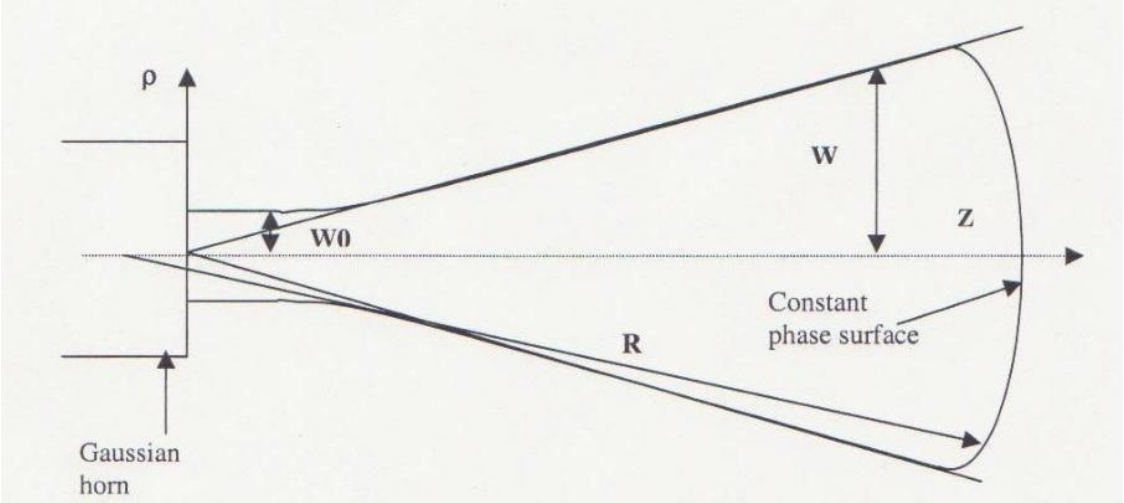

Figure 2.1.1: Gaussian beam radius w(z) spreading with propagation. The spreading of the beam radius is exaggerated here. The center of the phase surface sphere always occurs for $z < 0$.

where

$$w(z) = w_0 \left[1 + \frac{z^2}{z_0^2}\right]^{1/2}, \tag{2.1.8}$$

$$\Phi(\rho, z) = exp\left(-j\left[kz + \frac{k\rho^2}{2R(z)}\right] - T(z)\right). \tag{2.1.9}$$

Here E_0 is the amplitude constant, ρ is the cylindrical radius, $w(z)$ is the beam radius at propagation distance z, and $\Phi(\rho, z)$ is the phase function of the wave. The phase function is characterized by the radius ρ, the wave number k, the radius of curvature $R(z)$, a phase term $T(z)$, and the characteristic length z_0.

$$R(z) = z + \frac{z_0^2}{z^2}, \tag{2.1.10}$$

$$T(z) = \tan^{-1}\frac{z}{z_0}, \tag{2.1.11}$$

$$z_0 = \frac{kw_0^2}{2}, \tag{2.1.12}$$

2.2 Fourier Transform Method

Plane-wave spectrum analysis allows for the modeling of Gaussian beams by using the Fourier transform. This method of propagation is a straight forward for propagating beams in free space by only requiring the fields to be calculated at the desired propagation distance. Additionally it is made computationally simpler by the application of the Fast Fourier transform function. Furthermore, only Gaussian beams that have amplitude variation in one transverse direction are considered.

A Gaussian beam may be represented as an ensemble of plane waves. For a beam traveling with $\boldsymbol{k} = \hat{\boldsymbol{x}}k_x + \hat{\boldsymbol{z}}k_z$ where $k_z \gg k_x$ and with y polarization, the E field of a single plane wave may be written as

$$\boldsymbol{E} = \hat{\boldsymbol{y}}\, A\, exp(-jk_x x - jk_z z), \tag{2.2.1}$$

where $k_x^2 + k_z^2 = k^2$, with $k = \omega\sqrt{\mu\varepsilon}$. Using an ensemble of plane waves, the E field of the Gaussian beam is expressed as

$$\boldsymbol{E}(x,z) = \hat{\boldsymbol{y}} \int_{-\infty}^{+\infty} dk_x\, A(k_x)\, exp(-jk_x x - jk_z z) \tag{2.2.2}$$

with $k_z = \sqrt{k^2 - k_x^2}$. To obtain the expression for $A(k_x)$, Eq. 2.2.2 is set equal to the expression for a Gaussian E field at $z = 0$. The expression in Eq. 2.2.2 is the Fourier transform of the term $A(k_x)$ so in order to find $A(k_x)$, the inverse Fourier transform is carried out.

$$\int_{-\infty}^{+\infty} dk_x\, A(k_x)\, exp(-jk_x x) = E_0 \exp(-x^2/w_0^2) \tag{2.2.3}$$

$$A(k_x) = \frac{1}{2\pi}\int_{-\infty}^{+\infty} dx\ E_0 \exp(-x^2/w_0^2)\, exp(+jk_x x) \tag{2.2.4}$$

$$= \frac{E_0 w_0}{2\sqrt{\pi}} \exp\left(\frac{-w_0^2 k_x^2}{4}\right)$$

After obtaining the amplitude term $A(k_x)$, it is substituted into Eq. 2.2.2 to determine the total field of the beam,

$$\boldsymbol{E}(x,z) = \hat{\boldsymbol{y}}\frac{E_0 w_0}{2\sqrt{\pi}}\int_{-\infty}^{+\infty} dk_x \ \exp\left(\frac{-w_0^2 k_x^2}{4}\right) exp(-jk_x x - jk_z z) \qquad (2.2.5)$$

In order for the expression to remain bounded as z approaches infinity, the condition $k_x > k$ must hold so that $k_z = -j\sqrt{k_x^2 - k^2}$. To find an analytical solution to Eq. 2.2.5 a change of variables must be made. By setting $k_x = ku$ where $dk_x = kdu$ Eq. 2.2.5 yields

$$\boldsymbol{E}(x,z) = \hat{\boldsymbol{y}}\frac{E_0 w_0}{2\sqrt{\pi}}\int_{-\infty}^{+\infty} du \ \exp\left(\frac{-k^2 w_0^2 u^2}{4}\right) exp\left(-jkux - jk\sqrt{1-u^2}z\right). \qquad (2.2.6)$$

To calculate analytically the assumption that $kw \gg 1$ must be made. This assumption states that the cross section for the Gaussian beam must be many wavelengths wide. For a large number of beams of interest this is the case. For this case the first exponential function is negligible except for where u is very small compared to unity. From this the square root factor in the second exponential can be approximated by $(1 - u^2/2)$. Now Eq 2.2.6 becomes

$$\boldsymbol{E}(x,z) = \hat{\boldsymbol{y}}\frac{E_0 w_0}{2\sqrt{\pi}}\int_{-\infty}^{+\infty} du \ exp(-p^2u^2 + qu + c) \qquad (2.2.7)$$

with

$$p^2 = \tfrac{1}{4}k^2 {w_0}^2 - \tfrac{1}{2}jkz \qquad (2.2.8)$$

$$q = -jkx \qquad (2.2.9)$$

$$c = -jkz \qquad (2.2.10).$$

Integrating Eq 2.2.7 analytically yields

$$\boldsymbol{E}(x,z) = \hat{\boldsymbol{y}}\frac{E_0 k w_0}{2p} e^{q^2/4q^2} e^{-jkz}$$

$$= \hat{\boldsymbol{y}}\, E_0 \frac{1}{\sqrt{1-j\frac{z}{z_0}}} e^{-jkz} exp\left[\frac{-x^2}{{w_0}^2\left(1+\frac{z^2}{z_0^2}\right)}\left(1+j\frac{z}{z_0}\right)\right]. \qquad (2.2.11)$$

The exponential terms dominate the phase and amplitude of the wave in Eq. 2.23 when $z \gg z_0$. Similarly to the paraxial approximation above the beam width when the propagation distance is much more than the characteristic length, $w(z) = w_0 z/z_0$. The phase of the field is given by

$$phase = -k\sqrt{k_z} - \frac{x^2 z_0}{w_0^2 z} + \frac{\pi}{4}. \qquad (2.2.12)$$

While an analytical expression was obtained for the Gaussian beam using the Fourier transform, this expression in Eq. 2.2.11 is limited by the assumptions made in simplifying the integral just as the paraxial solution is limited in its analytical expression. However, by implementing the Fast Fourier Transform (FFT) solver it was possible to compare the analytical approximate solution to the numerical solution.

A 110 GHz Gaussian beam was propagated in the near and far field to distances that were multiples of the characteristic length, z_0. In these simulations the far-field was designated as $100z_0$. The phase and amplitude of both transverse electric field, $\mathbf{E_t}$, and the longitudinal field, $\mathbf{E_n}$, were investigated. For each simulation the initial waist radius was specified as a factor, g of the wavelength ranging from 0.5 to 5.0. The agreement between the paraxial approximation and the FFT method of narrow initial waist beams, $g < 1$, was of particular interest.

Overall there is very good agreement between the FFT propagation method and the paraxial approximation. The electric field amplitude of both the transverse electric field, E_x,

Table 2.2.1: Coupling Coefficient Between FFT Propagated Gaussian Beam and Paraxial Approximation Gaussian Beam Solution

		Propagation Distance (z/z_0)			
		1	2	3	10
Initial Beam Waist (w_0/λ)	.5	0.99	0.99	0.98	0.92
	.75	0.99	0.99	0.99	0.97
	1	1	1	1	1
	3	1	1	1	1

are shown in Fig. 2.2.1 and the longitudinal electric field, E_z, are shown in Fig. 2.2.2. The coupling coefficients between the FFT propagated beam and the paraxial approximation can be seen in Table 2.2.1. There is a discrepancy between the beams at initial beam waist radii of less than λ but this was expected because the assumptions of the paraxial approximation are no longer as valid.

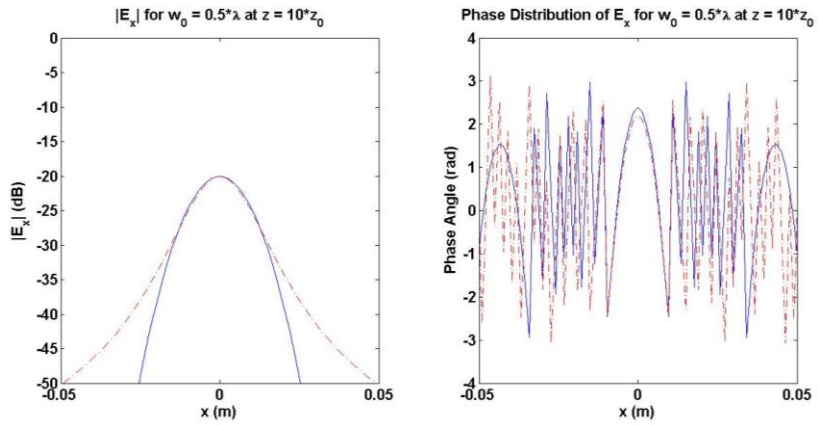

a)

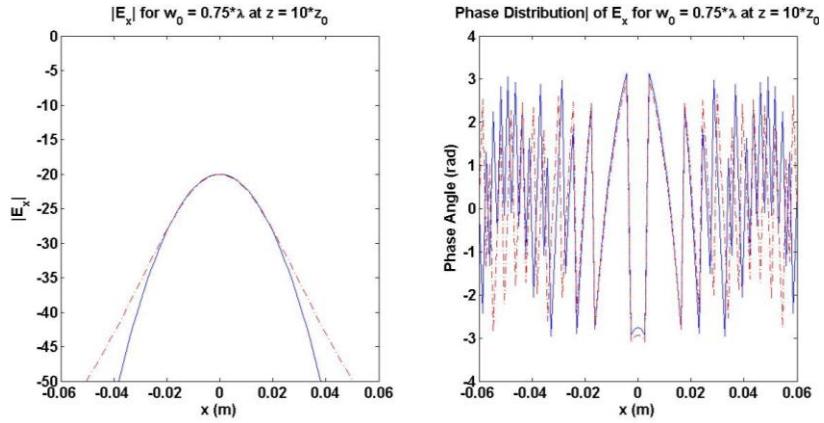

b)

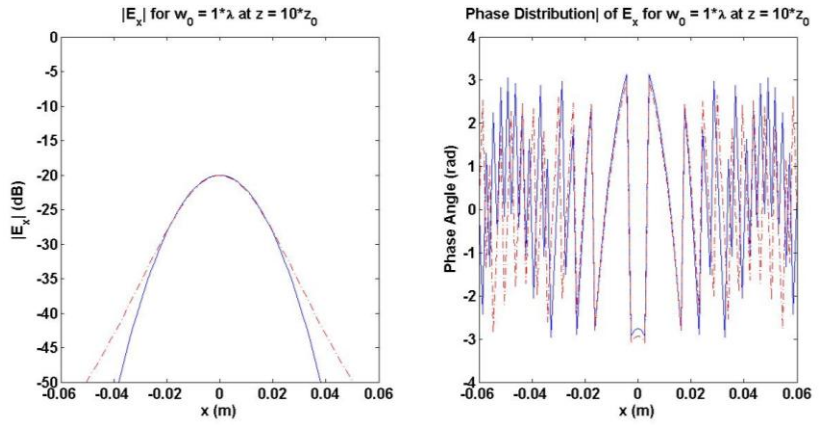

c)

Figure 2.2.1: Transverse electric field amplitude and phase angle at a propagation distance of $z = 10z_0$ for initial beam waste radii of a) $w_0 = .5\lambda$, b) $w_0 = 0.75\lambda$, and c) $w_0 = \lambda$.

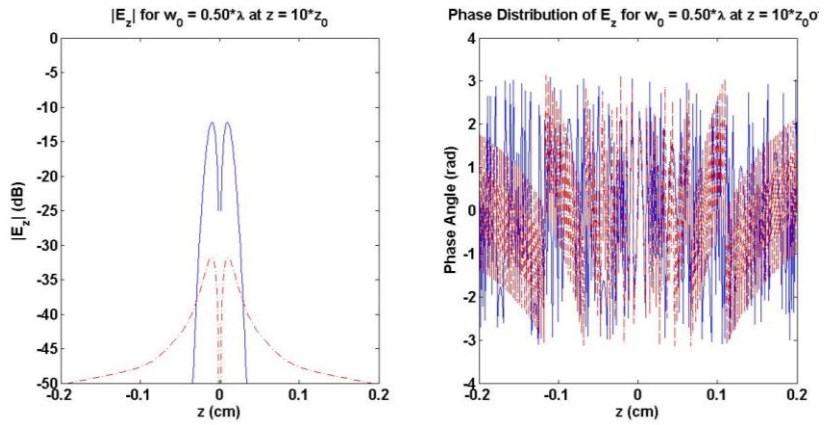

a)

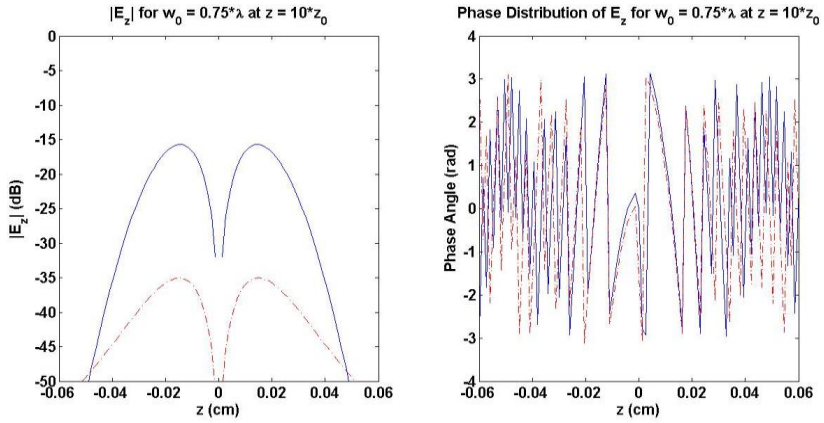

b)

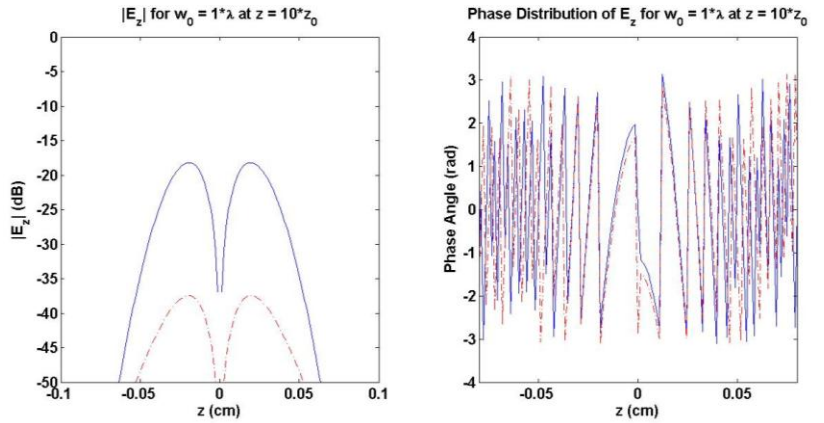

c)

Figure 2.2.2: Longitudinal electric field amplitude and phase angle at a propagation distance of $z = 10z_0$ for initial beam waste radii of a) $w_0 = .5\lambda$, b) $w_0 = 0.75\lambda$, and c) $w_0 = \lambda$.

2.3 Finite-Difference Time-Domain Method

Another method for treating Gaussian beam propagation is the Finite-Domain Time-Domain (FDTD) method. The FDTD method systematically models electromagnetic systems and has well understood accuracy and sources of error. While only the propagation of a Gaussian beam in free space is investigated and compared with other methods, the FDTD method would be useful in modeling domains containing scatters or dielectrics. The electric and magnetic fields must be calculated everywhere. This provides a complete visual representation but also computationally demanding.

The FDTD method is a direct solution of Maxwell's equations on a spatial grid or lattice. Starting with Maxwell's curl equations,

$$\frac{\partial \boldsymbol{H}}{\partial t} = -\frac{1}{\mu}\nabla \times \boldsymbol{E} - \frac{1}{\mu}(\boldsymbol{M_{source}} + \sigma^{*}\boldsymbol{H}) \tag{2.3.1}$$

$$\frac{\partial \boldsymbol{E}}{\partial t} = \frac{1}{\epsilon}\nabla \times \boldsymbol{H} - \frac{1}{\varepsilon}(\boldsymbol{J_{source}} + \sigma \boldsymbol{E}) \tag{2.3.2}$$

where $\boldsymbol{E}$ is the vector electric field, and $\boldsymbol{H}$ is the vector magnetic field, $\boldsymbol{M_{source}}$ is the vector magnetic current, $\boldsymbol{J_{source}}$ is the vector electric current, ε is the permittivity, μ is the permeability, $\sigma^{*}$is the magnetic conductivity, and σ is the electric conductivity. Next we consider a Gaussian beam with $E_y = 0$, $E_x = E_x(x,z)$, $E_z = E_z(x,z)$ and $H_y = H_y(x,z)$. Writing out the vector components of Eqs. 2.3.1 and 2.3.2 yields the coupled three dimensional wave equations.

$$\frac{\partial E_x}{\partial t} = \frac{1}{\varepsilon}\left[\frac{\partial H_y}{\partial z} - \left(\boldsymbol{J_{source_x}} + \sigma E_x\right)\right] \tag{2.3.3}$$

$$\frac{\partial E_z}{\partial t} = \frac{1}{\varepsilon}\left[\frac{\partial H_y}{\partial x} - \left(\boldsymbol{J_{source_z}} + \sigma E_z\right)\right] \tag{2.3.4}$$

$$\frac{\partial H_y}{\partial t} = \frac{1}{\mu}\left[\frac{\partial E_z}{\partial x} - \frac{\partial E_x}{\partial z} - \left(\boldsymbol{M}_{\boldsymbol{source}_y} + \sigma^* H_y\right)\right] \tag{2.3.5}$$

The incident electric field is polarized in the x-direction and it was assumed that there was no variation in the y-direction. This allows the reduction of the computation from three dimensions to two dimensions.

In order to obtain the needed update equations for implementing the FDTD method, second order centered finite-difference equations are used to approximate the derivatives in the two dimensional coupled equations given in Eqs 2.3.3-2.3.5.

$$\frac{\partial u}{\partial x}(i\Delta x, j\Delta y, k\Delta z, n\Delta t) = \frac{u^n_{i+1/2,j,k} + u^n_{i-1/2,j,k}}{\Delta x} + O[(\Delta x)^2] \tag{2.3.6}$$

$$\frac{\partial u}{\partial x}(i\Delta x, j\Delta y, k\Delta z, n\Delta t) = \frac{u^{n+1/2}_{i.j,k} + u^{n-1/2}_{i,j,k}}{\Delta x} + O[(\Delta x)^2] \tag{2.3.7}$$

The Yee algorithm is used as the basis for the transformation from the continuous domain and range to the discrete. This method is used in lossless materials where the magnetic and electric conductivities are equal to zero. The Yee algorithm solves for both the magnetic field and the electric field using Eqs. 2.3.3-2.3.5. This is an advantage over solving for either field independently and provides a more robust solution. Additionally, boundary conditions for the $\boldsymbol{E}$ field or $\boldsymbol{H}$ field can be modeled individually. An illustration of the Yee algorithm is depicted in Fig. 2.3.2 It is important to observe that each $\boldsymbol{H}$ field component is surrounded by four $\boldsymbol{E}$ field components and similarly each $\boldsymbol{E}$ field component is surrounded by four $\boldsymbol{H}$ field components.

The Yee algorithm manages to capture a discrete form of Maxwell's equations very well. It implements finite-difference expressions for the spatial derivatives that are used in the curl operators that have a central difference nature and are second order accurate.

Another important aspect is that if a material boundary is placed at a lattice coordinate access there is tangential continuity across the interface. Also, the $\boldsymbol{E}$ field and $\boldsymbol{H}$ field are divergence free when electric or magnetic charges are absent. The Yee algorithm is centered in time with respect to the $\boldsymbol{E}$ and $\boldsymbol{H}$ components. Therefore all of the $\boldsymbol{E}$ field calculations are done using the previous time step $\boldsymbol{H}$ field components. This process is fully explicit and simplifies the computational demand compared with some other methods.

Using these approximations Eqs. 2.3.3-2.3.5 become

$$E_x\big|_{i,k+1/2}^{n+1/2} = E_x\big|_{i,k+1/2}^{n-1/2} + \left(\frac{\Delta t}{\varepsilon \Delta z}\right)\left[H_y\big|_{i,k}^{n} - H_y\big|_{i,k+1}^{n}\right] \tag{2.3.8}$$

$$E_z\big|_{i-1/2,k+1}^{n+1/2} = E_z\big|_{i-1/2,k+1}^{n-1/2} + \left(\frac{\Delta t}{\varepsilon \Delta z}\right)\left[H_y\big|_{i,k+1}^{n} - H_y\big|_{i-1,k+1}^{n}\right] \tag{2.3.9}$$

$$H_y\big|_{i,k+1}^{n+1} = H_y\big|_{i,k+1}^{n} + \left(\frac{\Delta t}{\varepsilon \Delta z}\right)\left[E_x\big|_{i,k+1/2}^{n+1/2} - E_x\big|_{i,k+3/2}^{n+1/2} + E_z\big|_{i+1/2,k+1}^{n+1/2} - E_z\big|_{i-1/2,k+1}^{n+1/2}\right] \tag{2.3.10}$$

The time step is Δt and the grid spacing is given by Δx and Δz with $\Delta x = \Delta z$. Fig. 2.3.2 shows the grid cell used in the FDTD update equations.

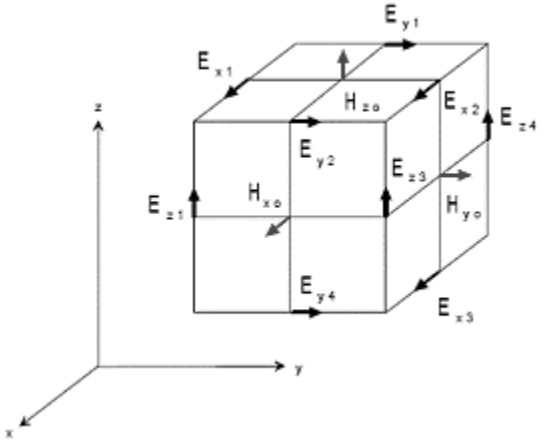

Fig. 2.3.2: FDTD grid cell. Taken from [6].

The FDTD method was compared against the FFT propagation method and the paraxial approximation. Fig. 2.3.3 shows the amplitude of the transverse electric field E_x and Fig. 2.3.4 shows the amplitude of the longitudinal electric field E_z. The transverse electric field shows relatively good matching to the paraxial approximation and the FFT method. Issues arise with comparison of the longitudinal field due to the low values of the field itself.

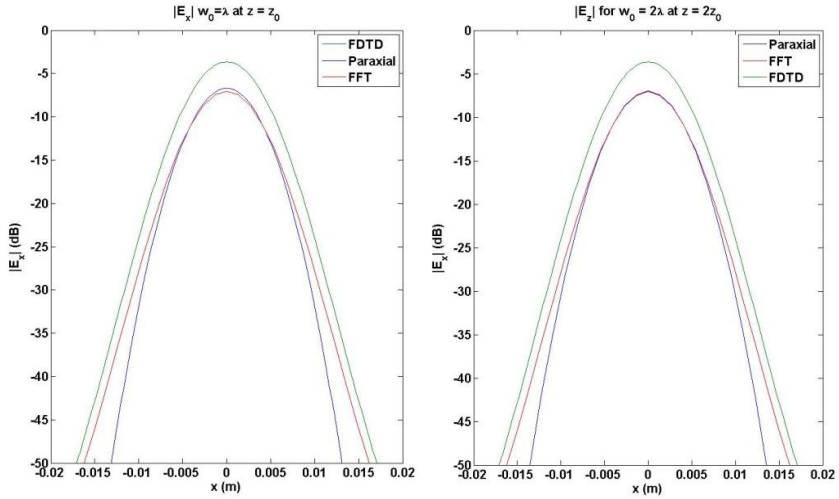

Figure 2.3.3: Transverse electric field magnitude obtained from FDTD method, FFT method, and paraxial approximation. FDTD amplitude is peak amplitude and FFT and paraxial amplitude are RMS.

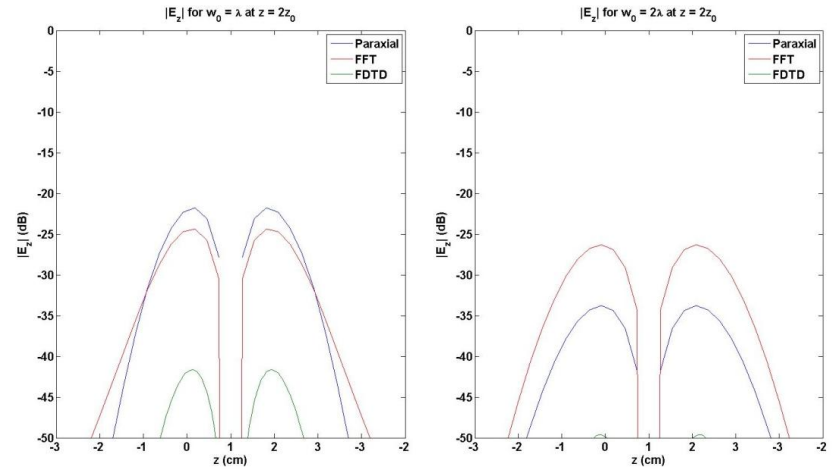

Figure 2.3.4: Longitudinal electric field magnitude obtained from FDTD method, FFT method, and paraxial approximation. FDTD amplitude is peak amplitude and FFT and paraxial amplitude are RMS.

Chapter 3

HSX Microwave Transmission System

In this chapter an analysis of the HSX microwave transmission system is performed. First the system as it is currently designed [3] with input from a smooth-wall Vlasov launcher is analyzed for its power efficiency and beam content. In order to increase the overall performance of the system, a second analysis was done using the perturbed-wall launcher designed by Ungku Fazri Ungku Farid [5] and suggestions on steps to redesign and alter the current HSX system are made.

3.1 HSX Microwave Transmission System Design

HSX is a quasihellically symmetric stellarator at the University of Wisconsin-Madison with a Varian 28 GHz TE_{02} gyrotron used for plasma heating and breakdown. Currently a smooth-wall Vlasov launcher, shown in Fig. 3.1.1, with a radius of 3.175 cm and a 2.66 ratio of operating frequency to cutoff frequency is used to feed a complex quasi-optical transmission line which feeds the stellarator. Our goal was to compare system outputs of the smooth-wall Vlasov launcher with a perturbed-wall launcher designed by Ungku Fazri Ungku Farid. Although the perturbed-wall launcher has increased Gaussian content and improved directivity the current HSX system was designed for the smooth-wall Vlasov launcher so we expect that system design changes would be necessary to make use of the improved output from the perturbed-wall launcher.

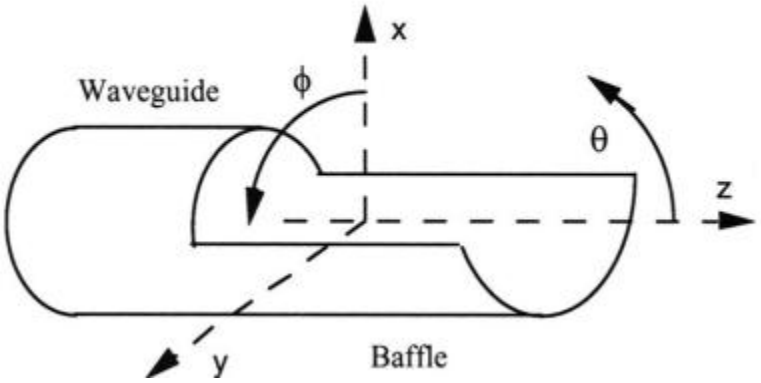

Figure 3.1.1: Generic picture of a TE_{0n} launcher with the corresponding coordinate system.

The HSX system consists of five design units: a quasioptical TE_{02}-to-TEM_{00} mode converter, a matching unit, a polarizer, a dual-mode (TE_{11}-TM_{11}) waveguide, and a quasioptical switch. Fig. 3.1.2 shows this system. The following work simulated the first three units of the system and focused on the input to the fourth. The HSX microwave transmission mirrors were designed for the system using a quasioptical and passive-high power microwave design techniques. Other TE_{0n} modes are present in the launcher but were not expected to propagate through the system due to the fact that the launcher angles that are different from the TE_{02} mode.

Inside the launcher waveguide the fields can be pictured as plane waves propagating down and bouncing off the walls inside off the waveguide. For understanding the geometrical optics of circular waveguides, it is important to understand the basics of Bessel functions. The Bessel function of the first kind, J_m, can be written as

$$J_m(x) = \frac{H_m^{(1)}(x)+H_m^{(2)}(x)}{2} \qquad (3.1.1)$$

Table 3.1.1 Matching Unit and Vlasov Mode Converter mirror parameters in HSX system. Taken from [3].

Mirror	**Curvature Radius (perp)**	**Curvature Radius (par)**	**Mirror Size (perp)**	**Mirror Size (par)**
M1	182.32	397.53	38.61	27.54
M2	-	205.06	22.51	32.17

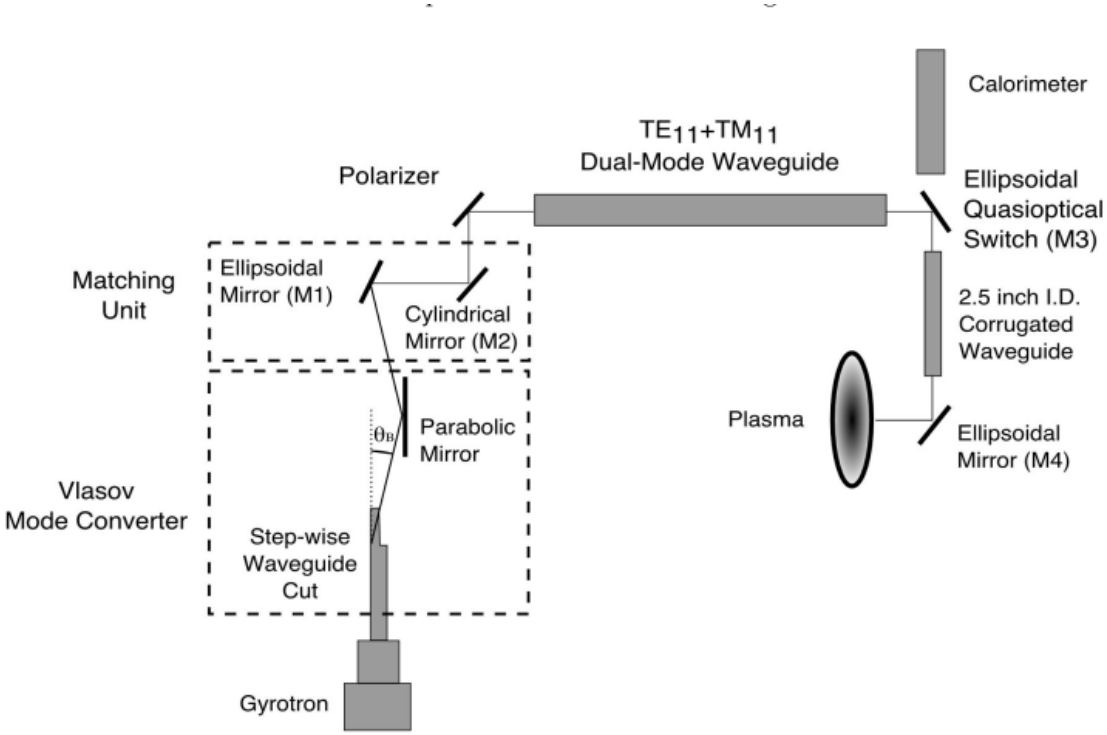

Fig 3.1.1: Hybrid transmission line for plasma heating in the HSX Stellarator. Taken from [3].

where $H_m^{(1)}(x)$ and $H_m^{(2)}(x)$ are the Hankel functions of the first and second kind respectively. Furthermore, these Hankel functions can be expressed as

$$H_m^{(1),(2)}(x) = J_m(x) \pm jY_m(x)\ , \qquad (3.1.2)$$

where $Y_m(x)$ is the Neumann function. The Hankel function can be approximated for large arguments where $x > m$ as

$$H_m^{(1),(2)}(x) = \sqrt{\frac{2}{\pi\sqrt{x^2-m^2}}}\, e^{j\left(\pm\sqrt{x^2-m^2}\mp m\cos^{-1}\left(\frac{m}{x}\right)\mp\frac{\pi}{4}\right)} \qquad (3.1.3)$$

From Eq. 3.1.3 only the phase components are of interest and the phase correction is close to the exact value as can be seen in Fig. 3.1.2. In Eqs. 3.1.1-3.1.3 x is a dummy variable that is replaced with $\beta_\rho\rho$ where $\beta_\rho\rho$ is equivalent to $\chi'_{mn}\left(\frac{\rho}{a}\right)$.

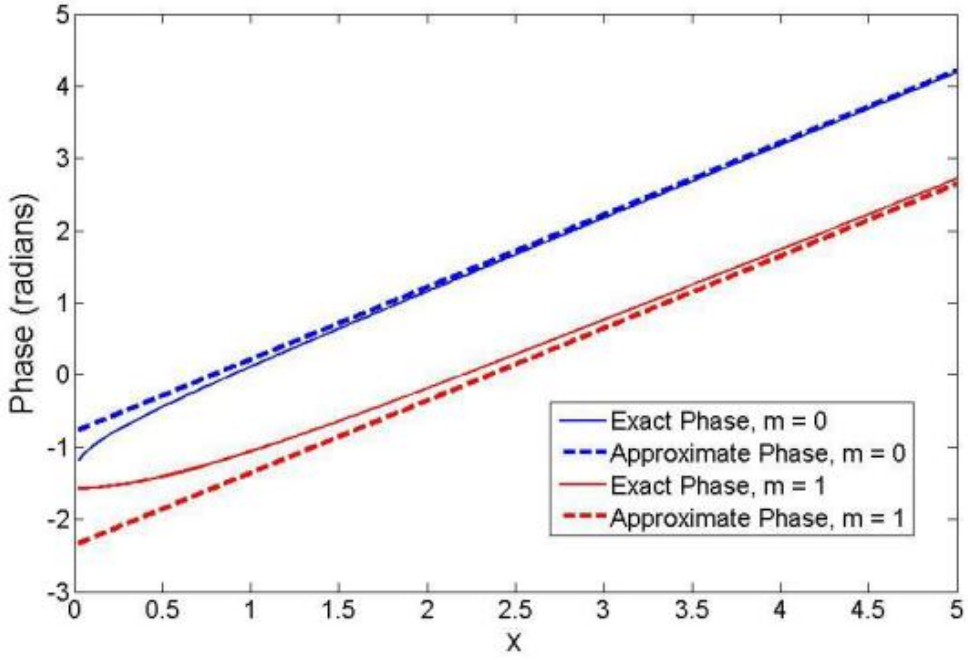

Fig. 3.1.2: Comparison between the phase values of the approximation of $H_m^{(1)}$ in Eq. 3.1.3 and the exact value of $H_m^{(1)}(x)$ for m = 1 and m = 1. From [5].

For propagating TE modes in the +z direction, the mode generating field is H_z and is given by

$$H_z^+(\rho,\phi,z) = J_m\left(\beta_\rho\rho\right)\left(A_{mn}e^{-jm\phi} + B_{mn}e^{+jm\phi}\right)e^{-j\beta_z z}\,. \qquad (3.1.4)$$

If Eq. 3.1.3 is inserted into Eq. 3.1.4 the phase component of the field becomes

$$arg\left(H_z^+(\rho,\phi,z)\right) \approx -\sqrt{\beta_\rho{}^2\rho^2 - m^2} + m\cos^{-1}\left(\frac{m}{\beta_\rho \rho}\right) - m\phi - \beta_z z + \frac{\pi}{4}. \quad (3.1.5)$$

The wavefront with a constant phase of K for the outgoing H_z field can be expressed as

$$arg\left(H_z^+(\rho,\phi,z)\right) - K = 0 \quad (3.1.6)$$

where it's gradient is

$$\boldsymbol{N}(\rho,\phi,z) = \nabla\left(arg\left(H_z^+(\rho,\phi,z)\right) - K\right) \approx \beta_\rho\sqrt{1 - \frac{m^2}{\beta_\rho{}^2\rho^2}}\,\hat{\boldsymbol{\rho}} + \frac{m}{\rho}\hat{\boldsymbol{\phi}} + \beta_z\hat{\mathbf{z}}. \quad (3.1.6)$$

Locally normals to the surfaces of constant phase can be visualized as a continuous beam of rays where the gradient of the wavefront represents the direction of the rays. This is shown in Fig. 3.1.3. On the waveguide walls where $\rho = a$, the gradient from Eq. 3.1.6 now becomes

$$\boldsymbol{N}(a,\phi,z) \approx \sqrt{\frac{\chi'_{mn}{}^2 - m^2}{a^2}}\,\hat{\boldsymbol{\rho}} + \frac{m}{a}\hat{\boldsymbol{\phi}} + \beta_z\hat{\mathbf{z}}\,. \quad (3.1.7)$$

From this it can be seen that the rays propagate at a fixed angle to the waveguide axis in the waveguide axis plane. This fixed angle is known as the axial bounce angle, θ_b. The derivation for the axial bounce angle comes from the gradient in Eq. 3.1.7 and can be described as

$$\cos(\theta_b) = \frac{\boldsymbol{N}(a,\phi,z)\cdot\hat{\mathbf{z}}}{|\boldsymbol{N}(a,\phi,z)||\hat{\mathbf{z}}|} = \frac{\beta_z}{\sqrt{\beta_\rho{}^2 + \beta_z{}^2}} = \frac{\beta_z}{\beta}, \quad (3.1.8)$$

$$\sin(\theta_b) = \frac{\beta_\rho}{\beta}. \quad (3.1.9)$$

For a radial cross section of the waveguide, it can be seen that the rays propagate normal to the wavefront in the transverse plane

$$\boldsymbol{N_t}(a,\phi,z) \approx \sqrt{\frac{\chi'_{mn}{}^2 - m^2}{a^2}}\,\hat{\boldsymbol{\rho}} + \frac{m}{a}\hat{\boldsymbol{\phi}} \quad (3.1.10)$$

In a similar manner the rays propagate at a fixed azimuthal angle, ψ where ψ can be found by

$$\cos(\psi) = \frac{\boldsymbol{N}(a,\phi,z)\cdot\hat{\boldsymbol{\Phi}}}{|\boldsymbol{N}(a,\phi,z)||\hat{\boldsymbol{\Phi}}|} = \frac{m}{\chi'_{mn}}. \quad (3.1.11)$$

From determining ψ, the angle that each ray could be shifted azimuthally between successive reflections on the waveguide walls can be described by 2ψ which is known as the azimuthal bounce angle.

It can be seen in Fig. 3.1.3 that all of the bouncing rays in the waveguide in the transverse plane are tangent to an inner circle. This inner circle is called the caustic circle and its radius is described by

$$\rho_c = a\cos\psi. \quad (3.1.12)$$

In the geometrical approximation of rays inside the waveguide no rays are able to propagate inside the caustic circle. However, the fields inside the circle are not zero and are found to decay radially inside the circle. For the TE_{0n} modes the caustic radius shrinks to zero.

For a given waveguide with fields operating at a set frequency, the axial bounce angle, θ_b, increases for each higher order TE_{mn} mode. This allowed the HSX system to be designed specifically for the TE_{02} mode and creates a situation where higher and lower ordered modes cannot propagate through the system. In addition to the bounce angle increase with higher order TE_{mn} modes, the bounce angle also decreases with frequency, f. This results in $\theta_b$becoming smaller the further a mode operates above the cut off frequency, f_c, and getting larger as a mode operates closer to the cutoff frequency. In the former case θ_b approaches 0˚ as the f approaches infinity and θ_b approaches 90˚ as f approaches f_c. A

parameter called the oversize factor indicates how far a mode operates from the cutoff frequency

$$OF = \frac{f}{f_c} = \csc\theta_b. \tag{3.1.13}$$

The rays' behavior described in the preceding paragraphs show that the rays completely bounce off segments of the waveguide walls. These segments of waveguide wall are referred to as Brillouin zones [7]. These zones are periodic and form parallelograms when unrolled onto a planar surface as can be seen in Fig 3.1.4. Brillouin zones are not unique and performing a geometrical translation or a rotation on a Brillouin zone will yield a Brillouin zone. An analogous description of Brillouin zones is as a set of cylindrical mirrors that reflect and propagate beams. It is important to note that these cylindrical mirrors border one another without overlapping and therefore form a complete circular waveguide. It can be seen that by removing one Brillouin zone from a circular waveguide that, according to this simple model, all of the fields exit through this hole and no fields will further propagate in the waveguide. Of course this is an idealized case and does not take into account diffraction. For the Vlasov launcher the last Brillouin zone at the end of the waveguide is removed so that the fields and power are propagated into free space [8]. The output radiation patterns of Vlasov launchers are difficult to work with and often perturbations on the waveguide walls and/or outside mirrors are needed to improve the radiation pattern. Fig. 3.1.5 shows the side view of a TE_{0n} launcher.

For rotating modes the helical line along which the rays bounce on the waveguide walls as shown in Fig. 3.1.4 can be described mathematically by the pitch angle, α_1 defined as

$$\alpha_1 = \tan^{-1}\left(\frac{\psi \tan\theta_b}{\sin\psi}\right) \tag{3.1.14}$$

The pitch distance, D_1 is defined as the distance a ray travels after having traversed a full 2πradians in the azimuth on the wave guide walls and is given by

$$D_1 = 2\pi a \cot\alpha_1. \tag{3.1.15}$$

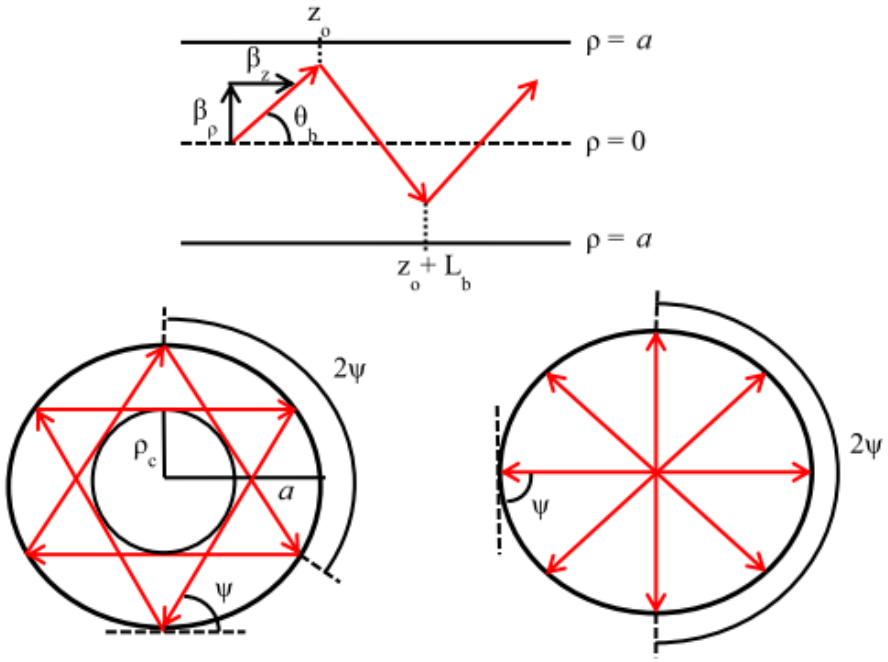

Fig. 3.1.3: Rays of a general TE_{mn} mode propagating inside a waveguide by bouncing along the waveguide walls, with the arrows representing the propagation direction. a) schematic representation of the side view (waveguide axis plane) of a generalized TE_{mn} mode. b) Radial cross-section (transverse plane) of a $TE_{22,6}$ mode where the value of $2\pi/2\psi$ is close to 3. c) Radial cross-sectionof a generalized TE_{0n} mode, where the value of $2\pi/2\psi$ is 2. From [5].

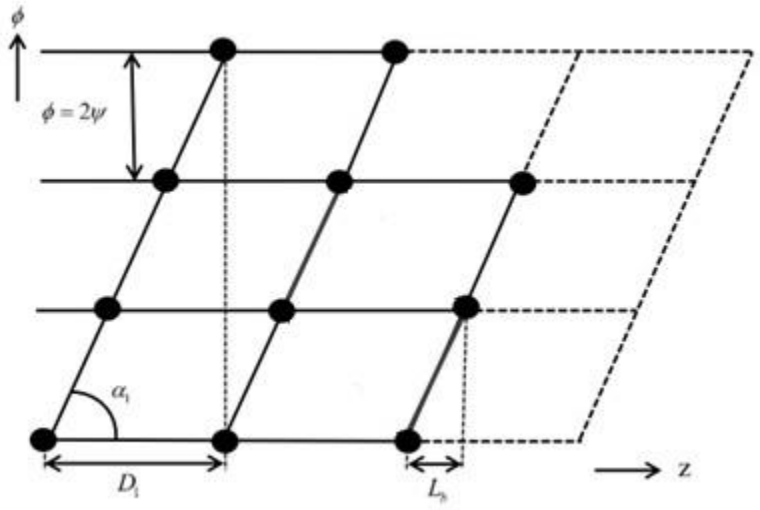

a) Brillouin zones for a $TE_{22,6}$ mode, where 2ψ is close to 120˚, and $2D_1/L_b$ is close to 3.

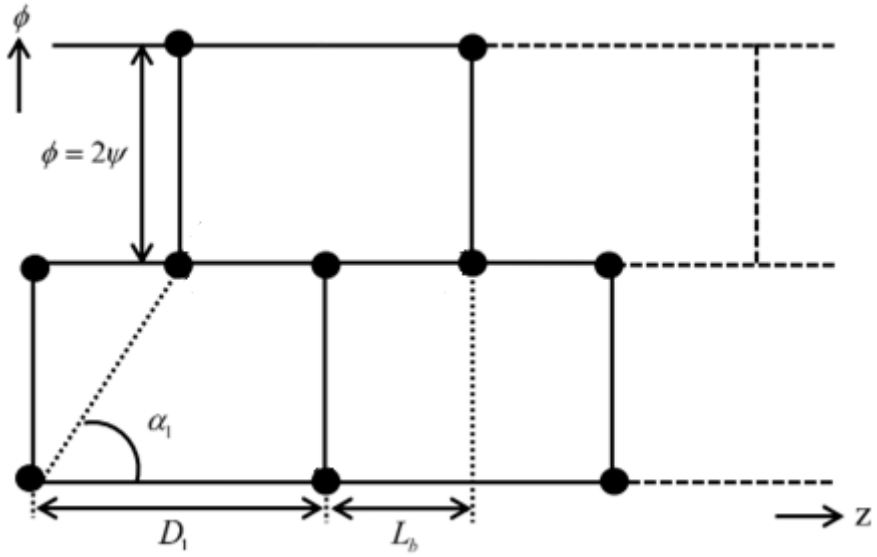

a) Brillouin zones for a TE_{02} mode, where 2ψ is exactly 180˚, and $2D_1/L_b$ is exactly to 2.

Fig. 3.1.4: Unrolled Brillouin zones for different TE modes. Broken lines indicate regions to be excised in a Vlasov launcher. Black dots trace out the rays bouncing location on the walls. Figures are not to scale and have been taken from [5].

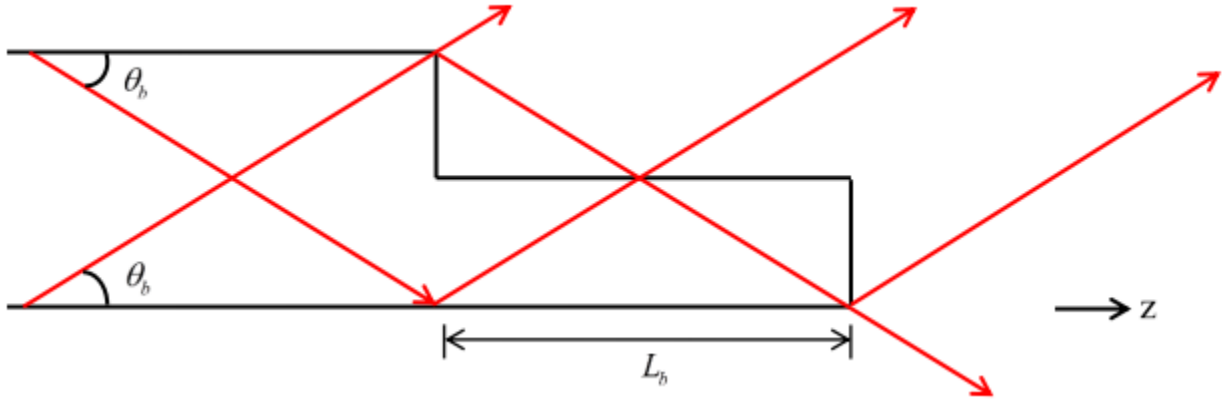

Fig. 3.1.5: Schematic representation of the side view of a rectangular-cut TE_{02} (non-rotating mode) launcher. Red arrows indicate propagating rays in or exiting the launchers. Figure is not to scale and is taken from [5].

The Vlasov mode converter was designed to convert the TE_{02} gyrotron output to a TEM_{00} Gaussian microwave beam. If the radius of the waveguide is given by a then the TE_{mn}/TM_{mn} mode can be understood by the caustic radius r_c , bounce angle θ_b, and bounce length L_B defined by

$$\theta_b = \sin^{-1} \kappa_{mn}/k \tag{3.1.14}$$

$$r_c = \mathrm{m}/\kappa_{mn} \tag{3.1.15}$$

$$L_B = 2\sqrt{a^2 - r_c^2}\cot\theta_b \tag{3.1.16}$$

$$\alpha = \begin{cases} \chi_{mn}/a & (TM_{mn}\ modes) \\ \chi'_{mn}/a & (TE_{mn}\ modes) \end{cases} \tag{3.1.17}$$

where k is the free space wavenumber and χ_{mn} and χ'_{mn} are the n^{th} zeros of $J_m(x)$ and $J'_m(x)$ respectively, the Bessel function of the first kind and its derivative. For the TE_{02} mode for a waveguide with $a = 3.175$ cm and a system frequency of 28 GHz, the values of these variables are $r_c = 0$, $\theta_b = 22.1°$, and $L_B = 15.63$ cm. The mode converter was implemented

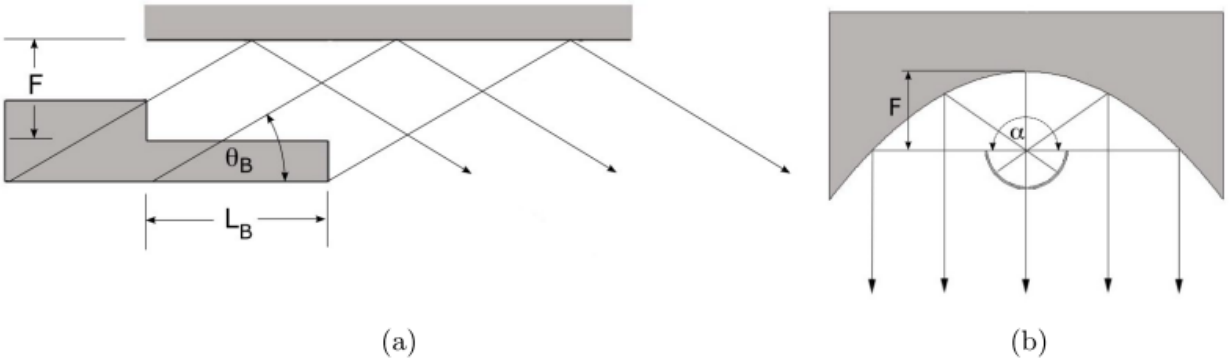

Figure 3.1.6: Vlasov converter: a) side view b) end view. Taken from [3].

using a step-wise cut wave guide and a parabolic mirror place at the focal distance, $F = 6.1$ cm, above the center of the waveguide as can be seen in Fig. 3.1.7

3.2 HSX Microwave Transmission System Analysis

The HSX transmission line system up to the TE_{11}+TM_{11} dual-mode waveguide was analyzed using Surf3d simulation software. Surf3d is a method-of-moments program created by Jeff Neilson at Lexam Research for calculating the electromagnetic field scattered from metal surfaces. The radiated field is calculated from arbitrary metal surfaces from an incident field from specified TE or TM waveguide source field modes. This section of the HSX system was chosen for analysis because the output of the Vlasov launcher is transformed and the most opportunity for power loss and possible improvement takes place within the Vlasov mode converter and the matching unit. In addition to the mirror geometry used to shape the beam, mirror M1 also consists of an integrated directional coupler made of twenty-five 1.2 mm diameter holes. Due to computational complexity this feature was not included in the simulated system. Another aspect of the system that was simplified was the polarizer that exists between M2 and the dual-mode waveguide. The polarizer was replaced with a simple planar mirror of similar geometry. It was assumed that minimal power loss takes place once the beam is input into the dual-mode waveguide.

It is evident that, while the geometrical design of the system is suitable, an improved system could be implemented using the perturbed-wall launcher. We expected the majority of power loss to take place initially from output of the Vlasov launcher and from the beam input to the waveguide. In addition to these two main factors it was also important to determine the amount of power lost due to spillover at M1, M2, and the polarizer.

At the input to the dual-mode wave guide it was important to consider two main factors, the total power in the beam and the Gaussian content of the beam. The total power in the beam was calculated by

$$P = \iint_A \boldsymbol{S} \cdot d\boldsymbol{A} \tag{3.2.1}$$

where $\boldsymbol{A}$ is simply the cross-sectional area of the dual-mode waveguide and $\boldsymbol{S}$ is the power density of the beam at the start of the waveguide given by

$$\boldsymbol{S} = \frac{1}{2} Re\{\boldsymbol{E} \times \boldsymbol{H}^*\}. \tag{3.2.2}$$

The Gaussian content of the beam was calculated through the power coupling coefficient c_p given by

$$c_p = \frac{|\iint E^*(u) f(u) du|^2}{\iint |E(u)|^2 du \iint |f(u)|^2 du} \tag{3.2.3}$$

A Gaussian beam input to the dual-mode waveguide is needed.

Using Surf3d we were able to propagate the beam from the launcher to the dual-mode waveguide input. A 28 GHz TE_{02} incident field was input at the start of the launcher. The overall profile of the resulting beam propagating through the system is shown in Fig. 3.2.1. The input field is shown in Fig. 3.2.2 and is the TE_{02} mode. From this simulation we were able to find the incident power at the entrance to the dual-mode waveguide to be 64% of the initial power and the Gaussian power coupling coefficient to be 0.86. A cross section of the beam seen at the dual-mode waveguide is shown in Fig. 3.2.3. It can be seen here that the beam profile is very nearly Gaussian. While a 64% efficiency is a positive result it is decreased further when TE_{01} and TE_{03} modes, which do not propagate to the dual-mode waveguide are accounted for. Considering the TE_{01} and TE_{03} modes which make up about

16% of the input beam in the real HSX transmission line system, the power efficiency of the system decreases to under 50%.

It is important to inspect the transmission system to see where power is lost from the TE_{02} beam. On quick inspection the main opportunities for power loss appear to be due to the Vlasov launcher output not propagated in the main beam, spillover from the mirrors, and the beam itself not being focused sufficiently into the waveguide. Out of these three we expect the amount of beam missing the waveguide and power lost in transmission from the Vlasov launcher to the parabolic mirror to be responsible for the majority of the power loss. While these should be the main factors, some spillover loss does occur.

The first step in understanding the power loss in the system was to check the power output from the Vlasov launcher that did not get directed into the parabolic mirror. To do this the fields on a cylinder that intersected the parabolic mirror at its parallel edges were simulated. While this does not find the fields on the parabolic mirror it does find the total power directed into the parabolic mirror. It was found that approximately 94% of the power output from the Vlasov launcher is incident on the parabolic mirror. However, not all of the power will be converted to a Gaussian beam and transmitted to the dual-mode waveguide. As can be seen in Fig. 3.2.5 there is a small portion of the output beam that is directed down and away from the parabolic mirror. This source of power loss is an inherent characteristic of the Vlasov launcher and could be reduced by introducing a more efficient launcher.

Moving through the system the total power in the beam was measured between mirrors M1 and M2. The total power determined in the beam was found to be 89% of the total input power. The profile of the beam can be seen in Fig. 3.2.6. In addition to the total

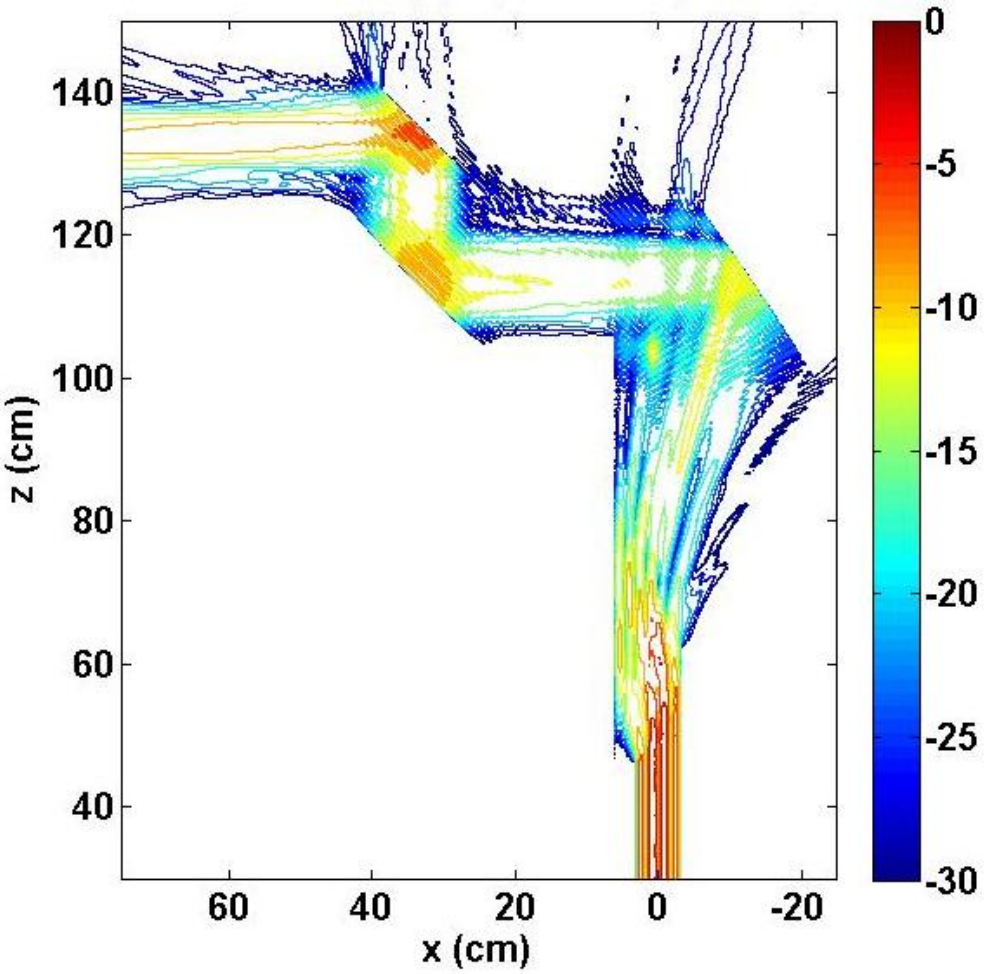

Fig 3.2.1: Side view of power density of TE_{02} mode beam propagated from the smooth-wall Vlasov launcher through the parabolic reflector, matching unit and polarizer of the HSX system.

power the power coupling coefficient was found to be 0.91. From the output of the Vlasov launcher the beam was transformed into a largely Gaussian beam after only the parabolic and ellipsoidal mirrors. However, if the total power measurement is restricted to the radius of the dual-mode waveguide from the center of the beam power efficiency decreased to 24 % with a power coupling coefficient 0.74. While mirror M1 does increase the Gaussian content of the beam it does not sufficiently narrow the beam to be input into the dual-mode waveguide.

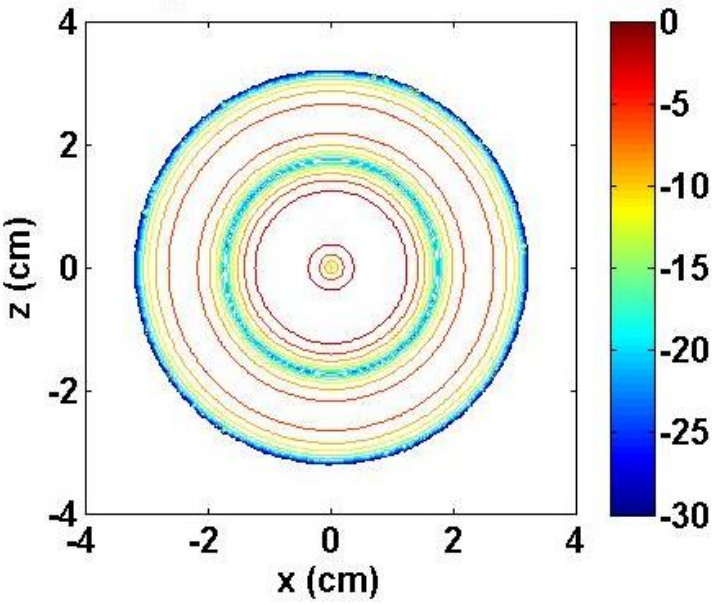

Figure 3.2.2: Cross-section of power density of TE_{02} mode input into smooth-wall Vlasov launcher.

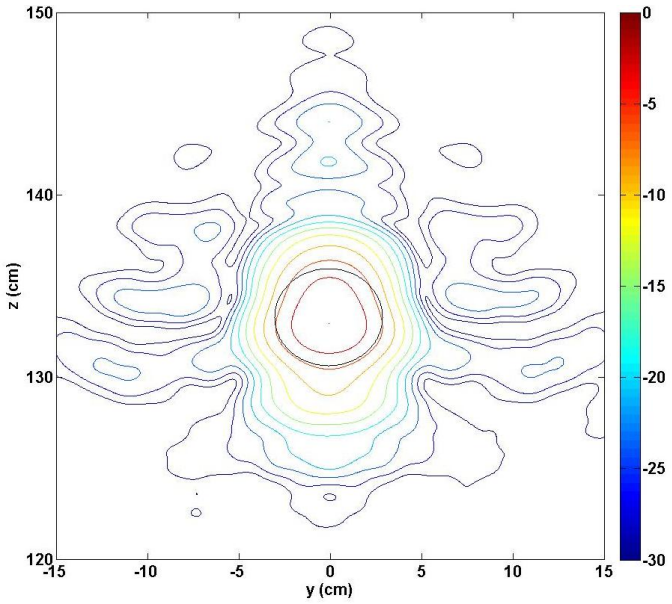

Fig. 3.2.3: Cross-section of power density of TE_{02} mode input to the smooth-wall launcher propagated to entrance of dual-mode waveguide in the HSX system.

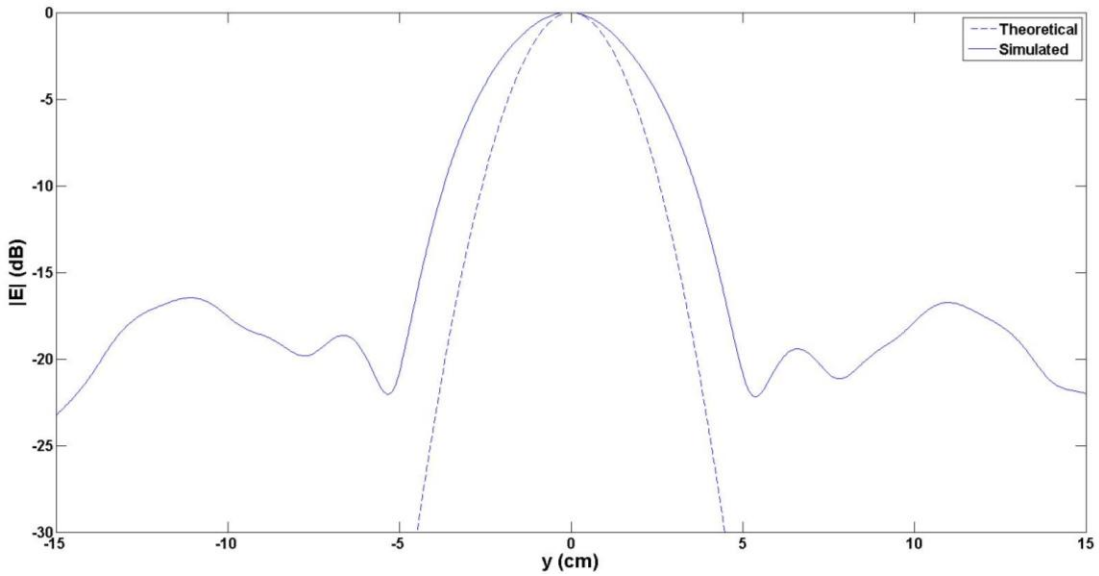

a) Electric field amplitude distribution along the horizontal axis for HSX system at the input to the dual-mode waveguide.

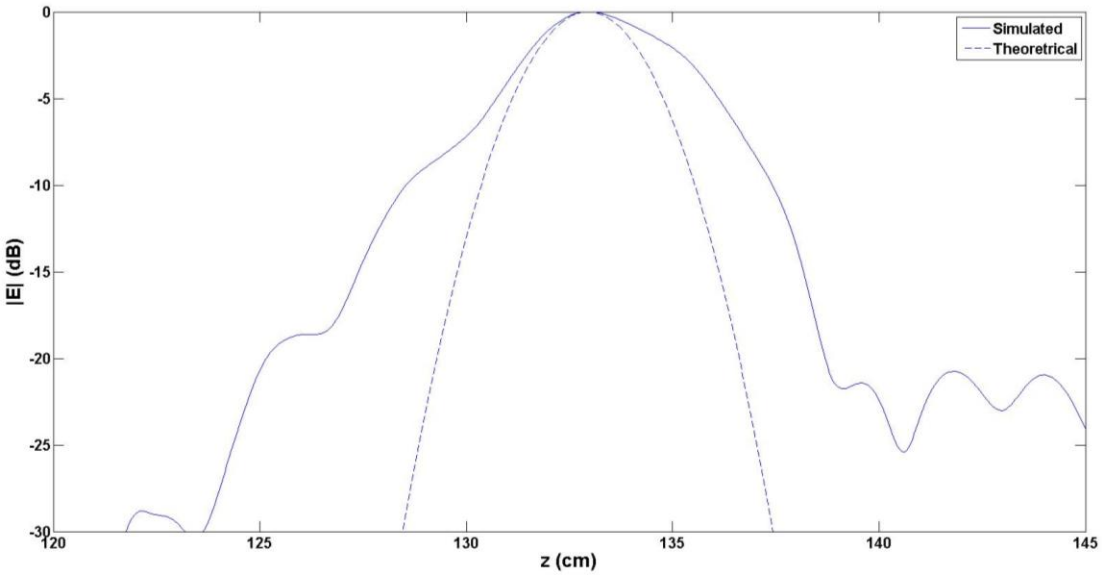

b) Electric field amplitude distribution along the vertical axis for HSX system at the input to the dual-mode waveguide.

Fig: 3.2.4: Theoretical and simulated distribution of electrical field amplitude of the HSX transmission system fed with the smooth-wall launcher at the dual-mode waveguide input.

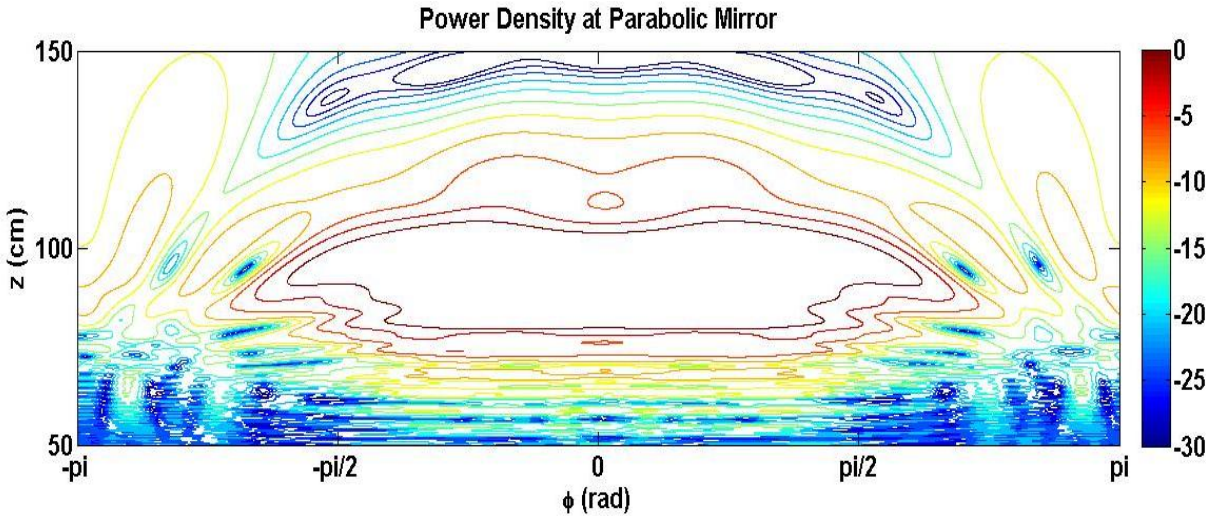

Figure 3.2.5: Power density of beam output from smooth-wall Vlasov launcher observed at ρ = 16.62 cm from center of the launcher.

Additionally because there is little observable beam divergence it can be approximated that a 6% power loss is due to spillover on mirror M1.

Investigating the beam above M2 it was determined that there was a slight power loss such that only 87% of the power remained in the beam. The cross-section of this beam can be seen in Fig. 3.2.7. The power coupling coefficient was also improved in both the beam from the observation between mirrors M1 and M2. In the beam the power coupling coefficient was found to be 0.92. Overall, mirror M2 is important in achieving a more focuses beam at the dual-mode waveguide.

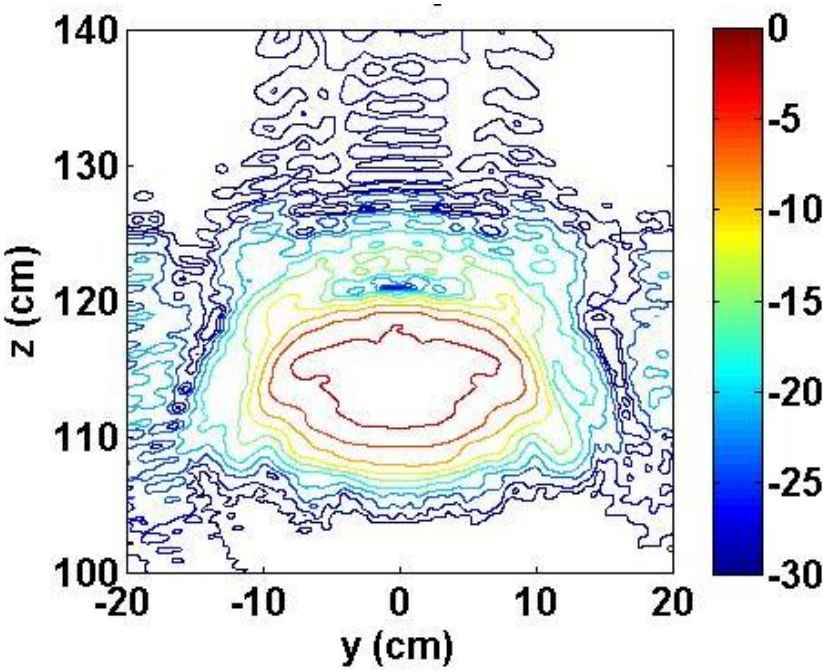

Figure 3.2.6: Cross-section of power density of beam propagated from smooth-wall Vlasov launcher in the HSX system observed between mirrors M1 and M2 at x = 15 cm.

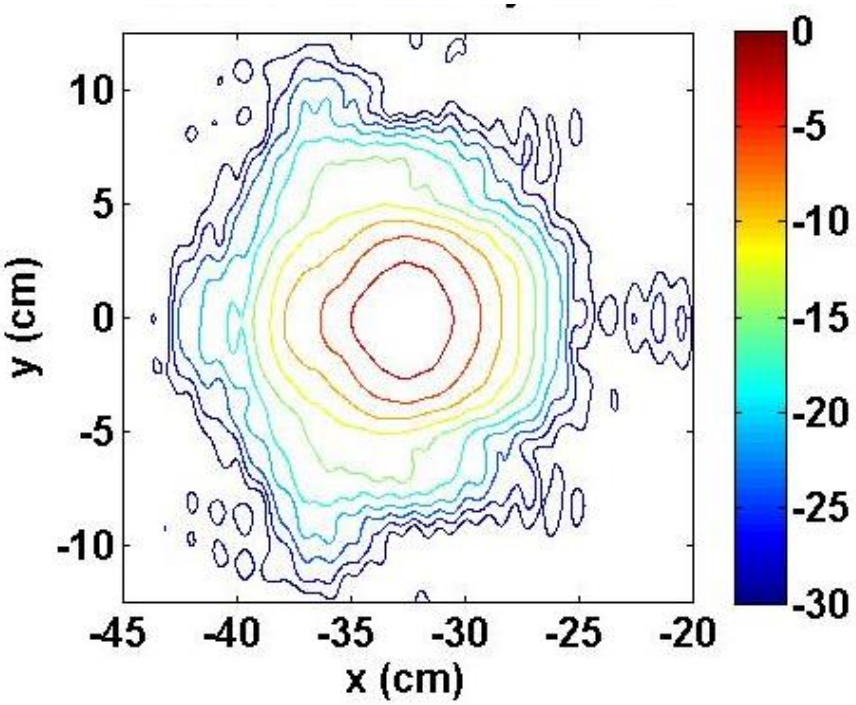

Figure 3.2.7: Cross-section of power density of beam propagated from perturbed-wall Vlasov launcher in the HSX system observed after reflection from mirror M2.

Investigating the power in the beam at the dual-mode waveguide revealed that the majority of power loss occurs between mirror M2 and the dual-mode waveguide. At the aperture of the dual-mode waveguide 67% of the power input to the HSX microwave transmission system is observed. Additionally, a power coupling coefficient of 0.94 was calculated to the target Gaussian beam described in [3]. Approximately 23% of the power in the beam that is reflected from M2 is not input into the dual-mode waveguide. If a narrower beam was formed from mirror M2 more power could be input into the waveguide but the beam might not have the desired waist for optimum coupling. Additional losses also occur at mirror M2 and the polarizer due spillover.

3.3 HSX System with Perturbed-Wall Launcher

While the HSX transmission line system is designed for a smooth-wall Vlasov launcher, it is precisely this launcher which introduces inefficiency and losses into the system that could be removed with the use of a launcher with better output. However, since the HSX system was designed for the output beam from a smooth-wall launcher, any other output beam may not propagate well through the system. Several main issues exist in the output radiation patterns of smooth-wall Vlasov launchers. The output of the smooth-wall Vlasov launcher in the far-field can be seen in Fig. 3.3.1.

First and probably most important is the main lobe. The output main lobe from the smooth-wall launcher is double-peaked and does not have the shape assumed by the ray-optics model. Only 77.5% of the power is in the main beam in the far-field. Additionally the azimuthal spread exceeds 180˚ and is therefore too large. The HSX system utilizes focusing and phase-correcting mirrors, but these introduce further loss into the system. Secondly, there are major diffraction losses and a large amount of the fields will be diffracted by the launcher cut and lost. Lastly the side lobes of the beam are substantial and result from the smooth-wall launcher radiation and from edge diffraction. It is very difficult to completely capture these large side lobes using most mirror systems and even when captured, they cannot be completely converted to a Gaussian beam with a simple mirror system. Perturbations can be applied to a smooth-wall Vlasov launcher to reduce these problems [9].

A perturbed-wall launcher was designed by Ungku Fazri Ungku Farid for possible use in the HSX system [5]. The launcher has a length of 62.49 cm (corresponding to three and a half Brillouin zones) with a maximum perturbation size of 12.82% of the radius. The

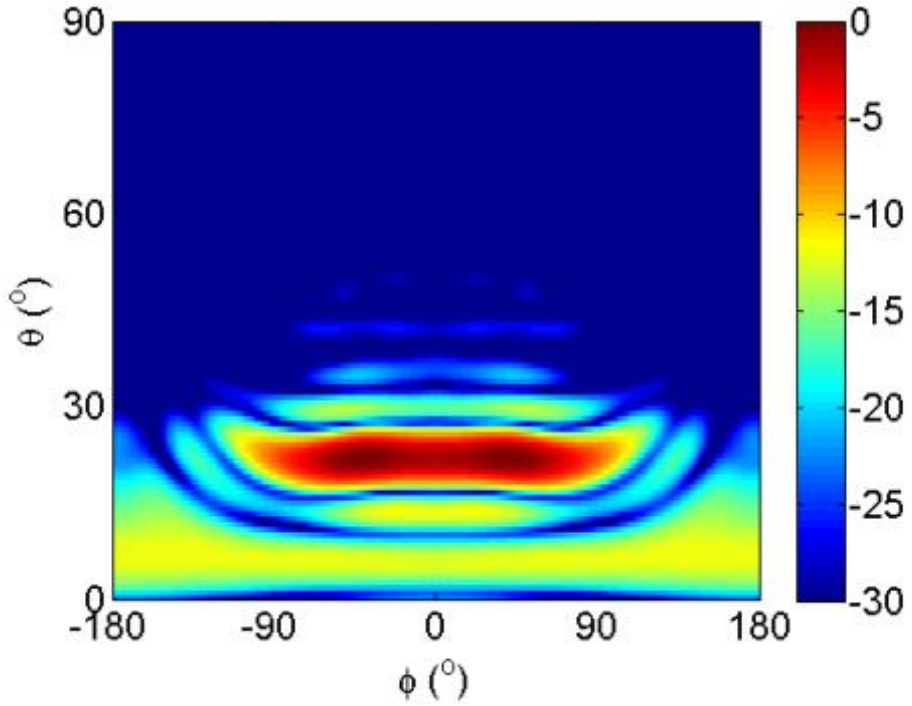

Fig. 3.3.1: The far-field pattern of $|E_\phi|$ co-polarization of the smooth-wall Vlasov launcher (in dB) obtained from Surf3d.

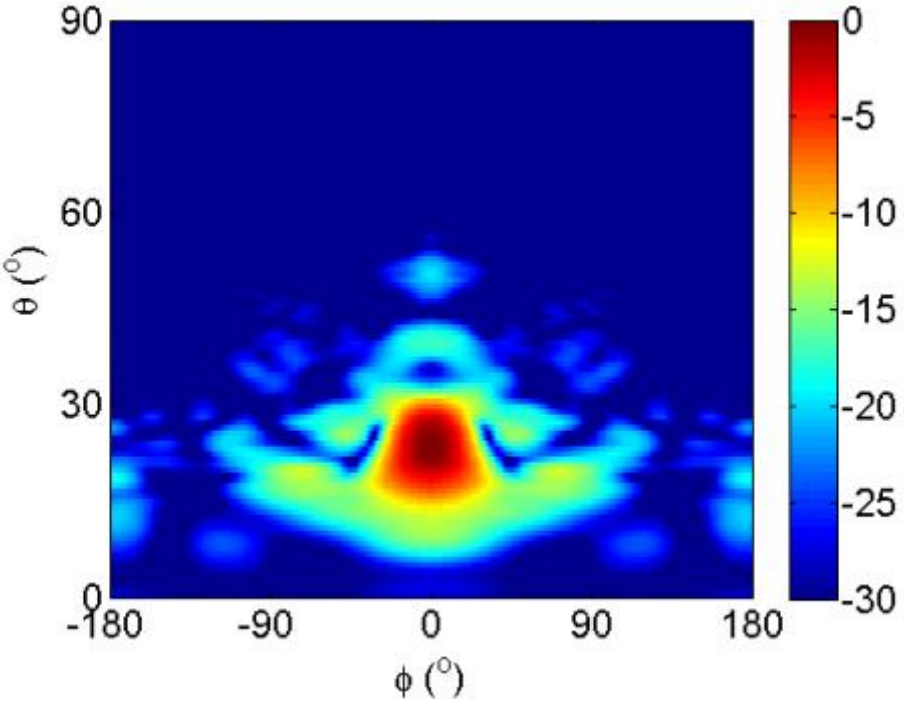

Fig. 3.3.2: The far-field pattern of $|E_\phi|$ co-polarization of the perturbed-wall HSX launcher (in dB) obtained from Surf3d.

Table 3.3.1: Summary of the Far Field Comparison of Launchers. Taken from [5].

Launcher	Co-polarization (E_ϕ)					Cross-polarization (E_θ)	
	Polar Exit Angle	Power in Main Lobe	Directivity, D_ϕ	10 dB Angular Spread		$\lvert E_\theta \rvert_{max}$	Total Power
				Azimuthal, $\Delta\phi$	Polar, $\Delta\theta$		
Smooth-wall	23.1˚	77.53%	21.4 dBi	205.8˚	9.1˚	-21.4 dB	<0.01%
Perturbed-wall	24.0˚	87.61%	24.4 dBi	63.14˚	16.5˚	-20.6 dB	<0.01%

co-polarization of the far-field in the perturbed-wall launcher can be seen in Fig. 3.3.2. The differences in the radiation output of the launchers is described in Table 3.3.1. One main aspect of the perturbed-wall launcher is that it does not output a good Gaussian beam with minimal side lobes as can be achieved with a longer perturbed-wall launcher. It should be noted that the polar exit angle changes slightly when perturbations are added to the launcher. This change in the polar exit angle was important and forced mirror M2 to be rotated slightly in order for the output beam to better propagate through the microwave transmission system. Overall the perturbations improved the percent of the power in the main lobe by 10% and improved the directivity by 3 dB. Additionally the azimuthal angular spread is decreased to less than a third of the value of the smooth-wall launcher. There is an increase in the polar spread by approximately 7.4˚.

Although the output beam from the perturbed-wall launcher has improved characteristics, it is important to determine if this beam will propagate through the current HSX microwave transmission system with no changes or minimal changes. Change in the

current system will entail significant expense and down time of the HSX stellarator. Using Surf3d, we were able to simulate a TE_{02} mode input into the perturbed-wall launcher and propagate the output beam through the HSX system. The propagating beam and the beam inside the launcher waveguide can be seen in Figs. 3.3.3 and 3.3.4. The only alteration to the system was to adjust mirror M1 such that it reflected the beam into M2. While this is not the original, system it was done to gain an understanding how the perturbed beam propagated. The HSX system was designed for the TE_{02}-mode input into the smooth-wall launcher so it was not expected that the same system would focus a completely different output beam effectively.

Due to the propagated beam undergoing a shift in the +z-direction the total dual-mode waveguide input power was measured at the center of the beam at z = 137.45 cm. At this position only 10% of the initial launcher input power was observed. As stated above this result was not unexpected due to the fact that the HSX system was not designed for the perturbed-wall launcher. The beam shape is shown in Fig. 3.3.6 and the beam profile is depicted in Fig. 3.3.5. As with the smooth-wall launcher it is important to go step by step through the system to understand where power is lost, especially considering whether redesigning the system to fit the perturbed-wall launcher could provide significant power efficiency.

At the launcher a simulation of the fields was done on a cylinder where the radius of the cylinder intersected the edges of the parabolic mirror parallel to the z-direction. This was done to calculate the total incident power on the parabolic mirror. Overall the result was very similar to the smooth-wall launcher. Here we saw that 95% of the power in the launcher waveguide was intercepted by the parabolic mirror. As can be seen in Fig. 3.3.7 there appears

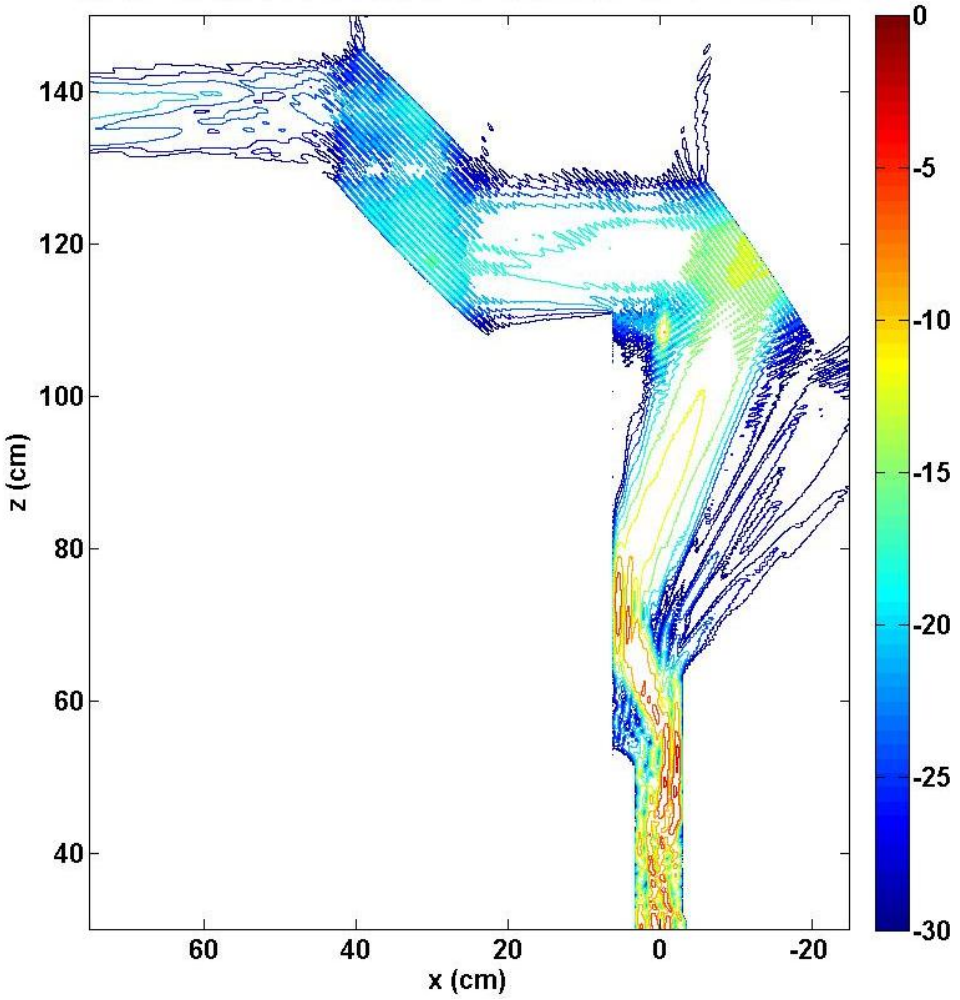

Figure 3.3.3: Side view of power density of TE_{02} mode beam propagated from the perturbed-wall launcher through the parabolic reflector, matching unit and polarizer of the HSX system.

to be a small lobe due to diffraction leaving the launcher 180˚ from the focal point of the parabolic mirror.

The overall power into the parabolic mirror was increased by the perturbed-wall launcher. However, we do expect to see a decrease in the performance of the system after

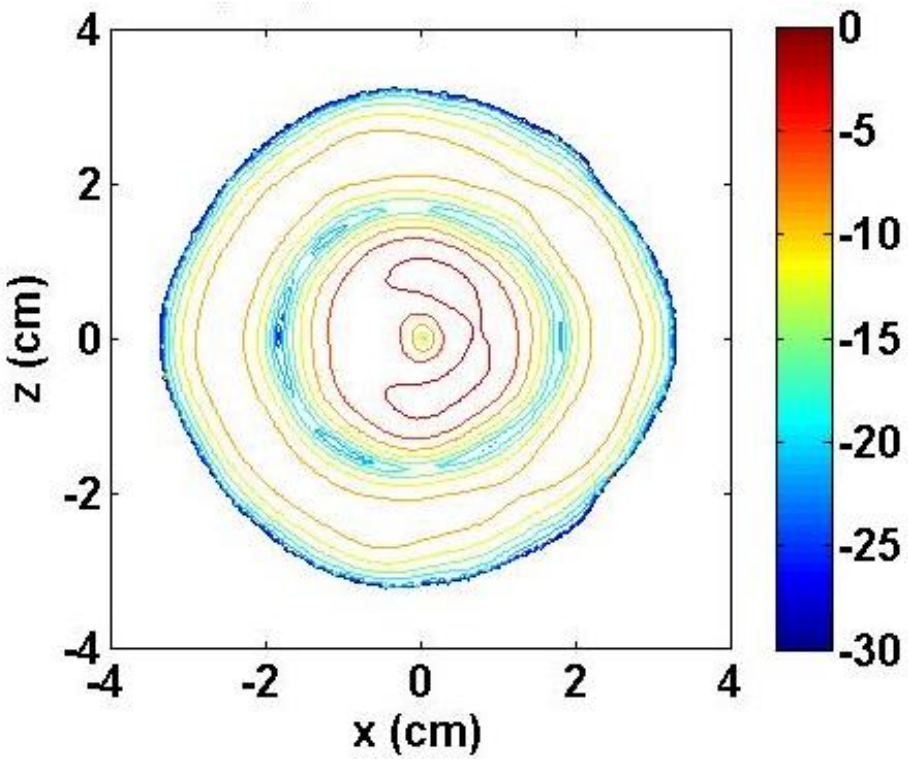

Figure 3.3.4: Cross-section of power density inside perturbed-wall HSX launcher before the baffle cut with TE_{02} source field.

mirror M1. With the initial orientation of mirror M1, the reflected beam was partially reflected back into the parabolic mirror. A large percentage of the beam that passed above the parabolic mirror missed the mirror M2. To understand how the system propagated the perturbed-wall beam, mirror M1 was adjusted by approximately 2˚. After making this adjustment the total power observed in the beam was 74% of the input power with a power coupling coefficient of 0.83 at the midpoint between mirrors M1 and M2. At this point between mirrors M1 and M2 the power measurement was restricted to only the radius of the dual-mode waveguide from the center of beam, the total power observed only decreased to 73% and the power coupling coefficient increased to 0.92. It can be seen in Fig. 3.3.8 that the beam has a desirable shape and the power is concentrated in the center of the main lobe. It

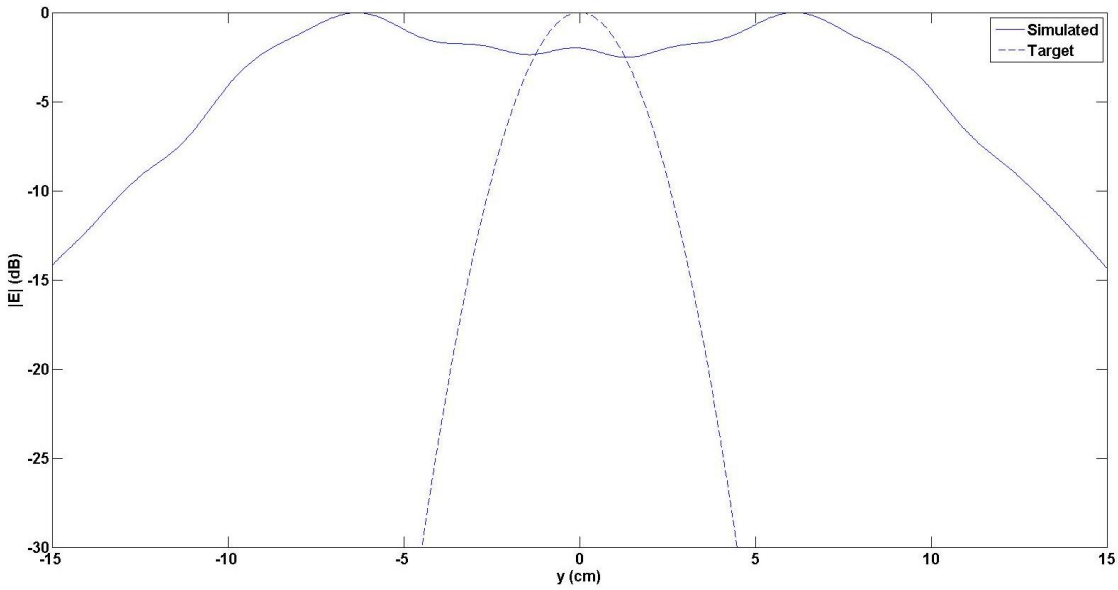

a) Electric field amplitude distribution along the horizontal axis for HSX system at the input to the dual-mode waveguide.

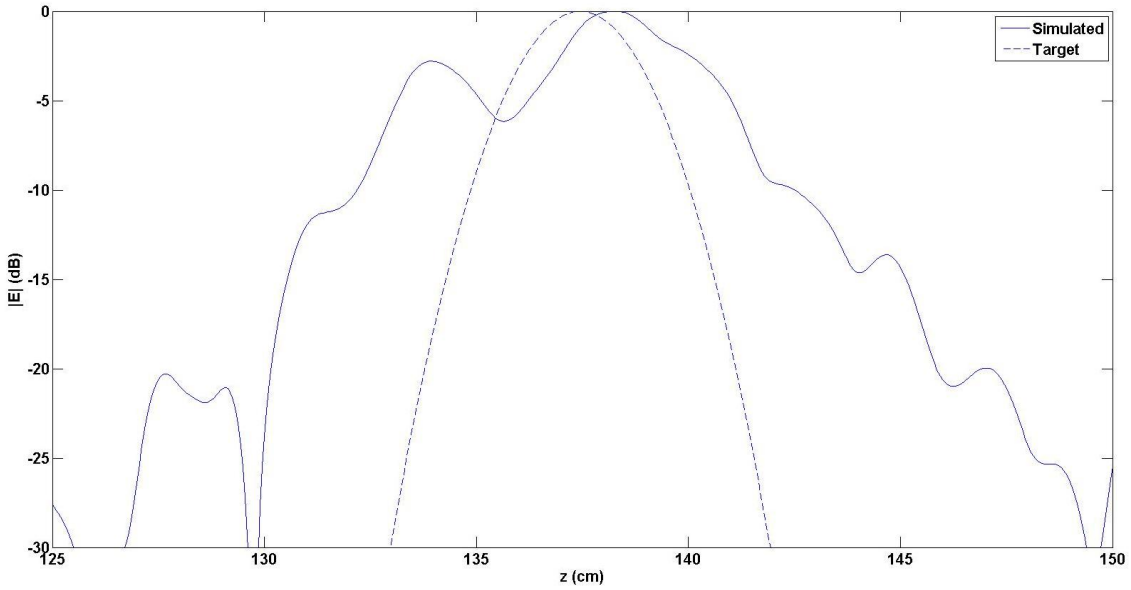

b) Electric field amplitude distribution along the vertical axis for HSX system at the input to the dual-mode waveguide.

Fig: 3.3.5: Distribution of electrical field amplitude of the perturbed-wall launcher feeding the HSX system at the dual-mode waveguide input.

can be seen from Figs. 3.3.3 and 3.3.8 that the majority of the power loss is through spillover from the beam incident on mirror M1from mirror M2 and can be seen in Fig. 3.3.9. There is remarkable decrease in the transmitted power after mirror M2. While the overall percentage of the input power in the total beam is 67% with a power coupling coefficient of 0.92 the beam is diverging and will not be focused properly at the dual-mode waveguide. This is not unexpected but demonstrates that mirror M2 does not properly focus the beam. It can also be seen from Fig. 3.3.3 that mirror M1 could potentially contribute to this problem by not focusing the beam properly on mirror M2.

The measured total beam power within the entrance to the dual-mode waveguide was only 10%. However, the total percentage of the input power in the beam at this point was found to be 53%. This is a large loss of almost half of the power in the beam. In addition to the total power, the power coupling coefficient was measure to be 0.74 for both the beam inside the waveguide entrance and the total beam. There is a large amount of power in the beam at this point that could be recovered with better focusing from mirror M2 to the waveguide. In addition to total power the Gaussian beam content needs to be improved. This is more intensive and would involve redesigning parts of the system, but could have the potential to reduce the number of mirrors and improve the overall power efficiency of the HSX system.

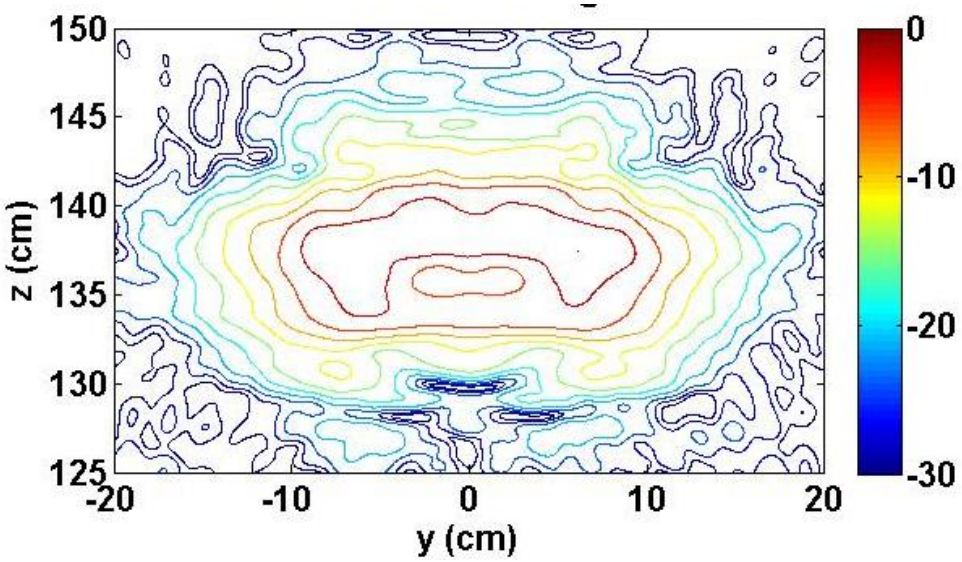

Figure. 3.3.6: Cross-section of power density of TE_{02} mode input to the perturbed-wall launcher propagated through HSX system to the input of the dual-mode waveguide launcher.

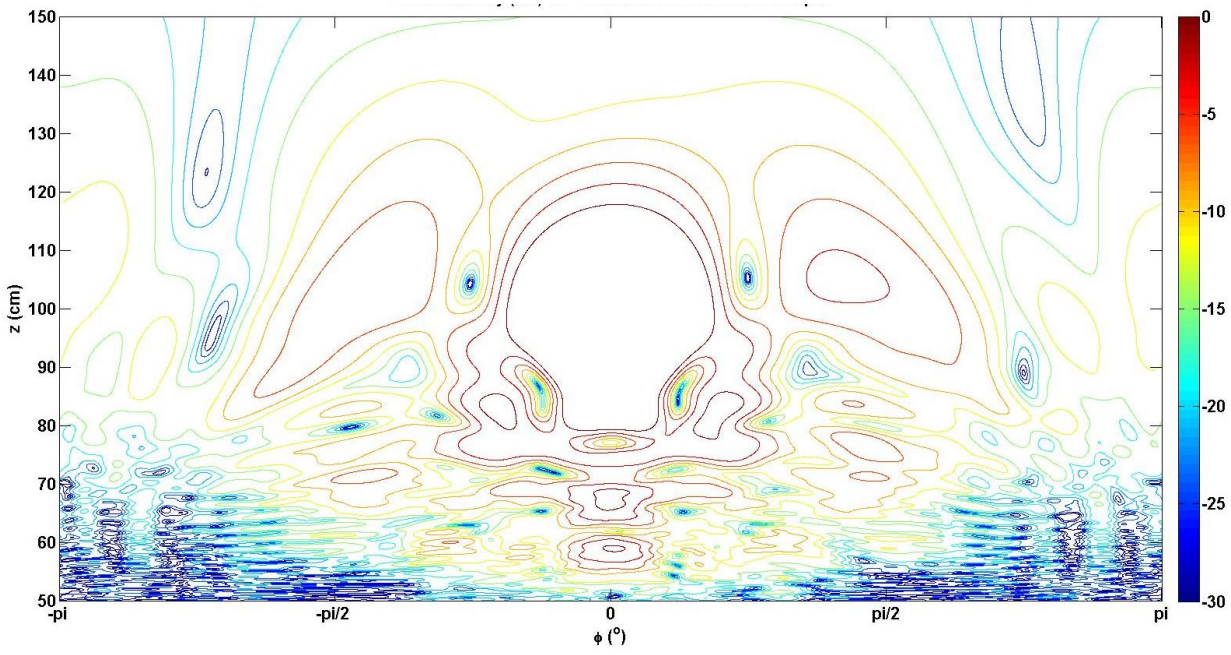

Figure 3.3.7: Power density of beam output from perturbed-wall launcher observed at ρ = 16.62 cm from center of the launcher.

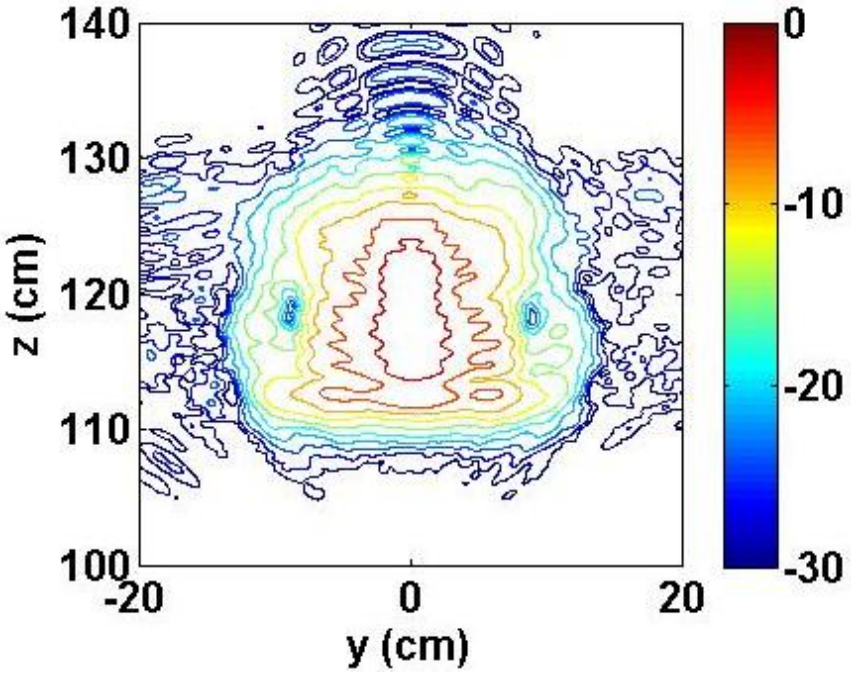

Figure 3.3.8: Cross-section of power density of beam propagated from perturbed-wall launcher in the HSX system observed between at the midpoint between mirrors M1 and M2.

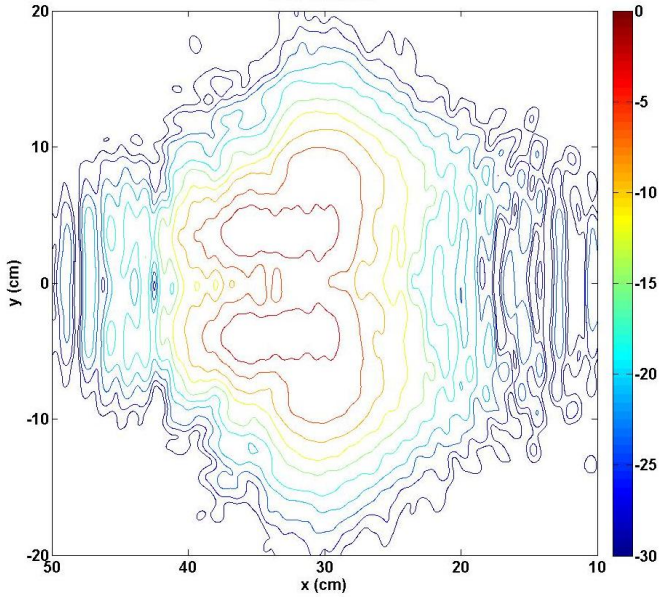

Figure 3.3.9: Cross-section of power density of beam propagated from perturbed-wall Vlasov launcher observed after reflection from mirror M2 in the absence of the polarizer.

Chapter 4

Conclusion

The Fourier Transform method and the Finite-Difference Time-Domain method both proved useful for propagating Gaussian beams. For initial waist radii that were close to or greater than one wavelength there was good agreement between these two methods and the paraxial approximation. Therefore for beams of with initial beam radii within this range it is a valid approximation that saves reduces computational cost. However, agreement between the FFT method and FDTD method and the paraxial approximation begin to breakdown for narrow initial waist radii. For beams with initial beam radii of less than a wavelength both methods prove valuable for modeling Gaussian beam propagation. The FFT method is less computationally demanding than FDTD so for beams propagating in free space it is a much more efficient method. However, the FDTD method allows complete design of the computational domain. If the Gaussian beam is incident on any surface the FDTD method is preferred.

Analyzing the TE_{02} mode propagated in the HSX system by both a smooth-wall Vlasov launcher and the perturbed-wall launcher revealed significant power loss from both launchers. However, the system is currently designed for the smooth-wall Vlasov launcher so the total percentage of input power observed at the dual-mode waveguide was found to be 63%. The majority of the power loss is introduced between mirror M2 and the dual-mode waveguide. Due to the fact that the HSX system was not designed for the perturbed-wall launcher it was not surprising that less than 10% of the total input power was seen at the dual-mode waveguide. In addition to the total power loss, the beam observed at the dual-mode waveguide has less Gaussian content than the beam from the smooth-wall launcher.

While the initial beam from the perturbed-wall launcher was more desirable it was transformed by the mirrors designed for the smooth-wall launcher. If the perturbed-wall launcher was implemented into the HSX system the mirrors would need to be redesigned. This could reduce the number of mirrors needed to shape the beam and improve the overall power efficiency of the system.

References

[1] G. Dammertz, S. Alberti, *et al*, "Development of a 140 GHz, 1-MW continuous wave gyrotron for the W7-X stellarator," *IEEE Trans. On Plasma Sci.*, vol. 30, no. 3, pp. 808-818, June 2002.

[2] J.P. Anderson, M. A. Shapiro, R.J. Temkin, I. Mastovsky, S.R. Cauffman, "Studies of the 1.5-MW 110 GHz gyrotron experiment," *IEEE Trans. On Plasma Sci.*, vol. 32, no. 3, pp. 877-883, June 2004.

[3] J. W. Radder, K.M. Liken, F.S.B. Anderson, and D.T. Anderson, "Hybrid transmission line for ECRH in the helically symmetric experiment," *Int. J. Infrared Millim. Waves*, vol. 29, no. 4, pp. 360-372, Apr. 2008.J. W.

[4] D.H. Martin and J.W. Bowen, "Long-Wave Optics," *IEEE Trans. Microw. Theory Techn.*, vol. 41, no. 10, pp. 1676-1690, October 1993

[5] U.F. Ungku Farid, "Theory and Algorithms for a Quasi-Optical Lancher Design Method for High-Frequency Gyrotrons," Ph.D. dissertation, ECE Dept., UW-Madison, Madison, WI, 2013.

[6] A. Taflove and S.C. Hagness, "Introduction to Maxwell's Equations and the Yee Algorithm," in *Computational Electrodynamics*, 3rd ed. Norwood: Artech House, Inc, 2005, ch. 3, pp. 51-106.

[7] A.A. Bogdashov and G. G. Denisov, "Asymptotic theory of high-efficiency converters of higher-order waveguide modes into eigenwaves of open mirror lines," *Radiophys. Quantum Electron.*, vol 49, no. 4, pp. 283-296, 2004

[8] S. N. Vlasov, L. I. Sagryadskaya, and M. I. Petelin, "transformation of a whispering gallery mode, propagating in a circular waveguide, into a beam of waves," *Radio Eng.*, vol 12, no. 10, pp 14-17, 1975.

[9] Q. Li, P.J. Sealy, and R.J. Vernon, "Preliminary work on a perturbed-wall Vlasov launcher for a TE_{0n} mode using surf3d," in *Joint 32nd Int. Infrared Millim. Waves Conf./15th Int. Terahertz Electron. Conf.*, Cardiff, UK, Sep. 2007.